

## First-principles study of the surface of silica and sodium silicate glasses

Zhen Zhang<sup>1,2</sup>, Walter Kob<sup>1</sup>, and Simona Ispas<sup>1,\*</sup>

<sup>1</sup>Laboratoire Charles Coulomb (L2C), University of Montpellier and CNRS, F-34095 Montpellier, France

<sup>2</sup>Center for Alloy Innovation and Design, State Key Laboratory for Mechanical Behavior of Materials,

Xi'an Jiaotong University, Xi'an 710049, China



(Received 16 January 2021; revised 10 April 2021; accepted 13 April 2021; published 6 May 2021)

We use *ab initio* molecular dynamics simulations to investigate the properties of the dry surface of pure silica and sodium silicate glasses. The surface layers are defined based on the atomic distributions along the direction ( $z$  direction) perpendicular to the surfaces. We show that these surfaces have a higher concentration of dangling bonds as well as two-membered (2M) rings than the bulk samples. Increasing the concentration of Na<sub>2</sub>O reduces the proportion of structural defects. From the vibrational density of states, one concludes that 2M rings have a unique vibrational signature at a frequency  $\approx 850\text{ cm}^{-1}$ , compatible with experimental findings. We also find that, due to the presence of surfaces, the atomic vibration in the  $z$  direction is softer than for the two other directions. The electronic density of states shows clearly the differences between the surface and interior and we can attribute these to specific structural units. Finally, the analysis of the electron localization function allows to get insight on the influence of local structure and the presence of Na on the nature of chemical bonding in the glasses.

DOI: [10.1103/PhysRevB.103.184201](https://doi.org/10.1103/PhysRevB.103.184201)

### I. INTRODUCTION

Developing glasses with tailored surface properties is an important step in many types of applications such as the production of ultrathin flexible displays and energy-efficient windows, catalysis technology, electronics, and biomaterials [1–7]. Among the problems one faces in the design of glasses with specific properties are the presence of surface defects which can lead to a dramatical drop of the mechanical strength or a strong alternation of the chemical reactivity of the samples. In spite of the considerable number of experimental and computational studies that have probed the surface properties of silicate glasses, we still lack atomistic insight how the glass composition affects the structure of such surfaces or the concentration of defects, or how the local structure of the surface influences the spectroscopic and electronic properties. Note that when we discuss here glass surfaces, we refer to surfaces that have been obtained by cooling the glass former from the melt, i.e., we do not consider the case in which the surface is produced by a fracture process [8,9].

Experimental techniques such as low-energy ion scattering (LEIS) spectroscopy, x-ray photoelectron spectroscopy (XPS), or atomic force microscopy (AFM) have provided information on surface composition and its microstructure [10–17]. The LEIS technique has, e.g., allowed to demonstrate that melt-formed surfaces of binary oxide glasses are depleted of the modifier atoms which seem to evaporate when the sample is still in the liquid state [12]. AFM measurements have allowed to probe the structural features of glass surfaces with atomic resolution, and thus to obtain structural information such as interatomic distances and grouping of atoms, but

the nature of the defects could not be determined [14–17]. Information on the surface structure can also be obtained from spectroscopic techniques such as infrared (IR) spectroscopy, nuclear magnetic resonance (NMR), extended x-ray absorption fine structure (EXAFS), or electron paramagnetic resonance (EPR) [18,19]. However, in order to obtain from such techniques information about the structural properties of the surface, it is usually necessary to make a hypothesis on the nature of the defects and/or to combine spectral, kinetic, and computational data, a task that is not straightforward at all [19,20].

Pure silica is the simplest silicate glass and because of its importance in industrial and engineering applications such as support medium for modern heterogeneous catalysts and biomolecules it has been widely studied in the past [4,21–23]. Experimental as well as theoretical studies have given evidence that the local structure of the outermost layer of silica surfaces consists of SiOSi bridges (called siloxane bridges) and SiO<sub>4</sub> tetrahedra bearing one or two OH groups [4,22]. Using appropriate heating and thermal treatment (above 700 °C), the concentration of these silanol groups can be reduced, allowing to generate partially or even fully dehydroxylated silica surfaces [24–28]. With the reduction of the surface hydroxylation, defective structures are generated, in particular strained two-membered (2M) rings, i.e., two tetrahedra that share an edge. The presence of this type of defect, completely absent in the bulk sample, was inferred from the appearance of certain features in the IR spectra, namely, two bands at 888 and 908 cm<sup>-1</sup>, and a shoulder at 932 cm<sup>-1</sup> [24–26,29]. These 2M rings are under high local stress and hence are considered to be important reactive sites capable to favor the functionalization of the surface as indicated by various experimental studies [20,27]. Other experiments indicate the existence of further local defects, such as undercoordinated

\*Corresponding author: simona.ispas@umontpellier.fr

silicon and nonbridging oxygen atoms, but their concentration and the way they modify the network are not known [28,30].

These experimental efforts have been complemented by computer simulation studies, pioneered by the classical molecular (MD) simulations of Garofalini and coworkers [31–33]. Using various types of interaction potentials, the surfaces of silica glasses were investigated in detail in order to identify the different structural features and in particular the concentration of the mentioned defects [34–41]. Although most of these studies did indeed report a finite concentration of the various local defect sites, the values did not match well the experimental data, likely because of the used protocol to generate the samples or the inaccuracies of the interaction potential. Similar investigations have also been carried out for surfaces of more complex glasses and it was found that their structure differed significantly from the one of the bulk system [42–45].

Note that most effective force fields used to carry out these simulations have been developed to describe the bulk properties of glasses. Therefore, it is far from obvious whether or not such classical MD simulations are able to give a quantitative correct description of the local structure of the surface since the arrangement of the atoms is very different from the one encountered in the bulk. This problem can be avoided by using an *ab initio* approach in which the forces are directly calculated from the electronic degrees of freedom [46]. This approach is thus not only more reliable, but in addition it also allows to determine the electronic signatures of the main structural features of samples with surfaces.

The goal of this work is thus to provide a detailed description of silicate glass surfaces in terms of their structural, vibrational, and electronic properties and to probe how these properties depend on the composition of the glass. The use of *ab initio* calculations will allow us to extract the spectroscopic and electronic signatures of the defective sites and in particular to understand how the presence of Na atoms affect the various properties. In most applications, silicate glass compositions contain alkali modifiers, and sodium is probably the element that is most commonly used [21]. However, even if the results and data discussed in the following do focus on sodium-containing systems, they should also give insight into the properties of the surface of glass-forming systems that contain other alkali modifiers.

The remainder of the paper is organized as follows: The next section gives details on the composition of the studied glasses, the protocol used to generate samples with surfaces, as well as on the adopted computational framework. In Sec. III we will present a description of the structural properties of the surface domain and compare these to the ones of the interior (bulklike) one. Subsequently, we will show and discuss the vibrational (in Sec. IV) and electronic (in Sec. V) properties of the studied compositions. Finally, the last section will summarize the conclusions and give perspectives of this work.

## II. SIMULATION DETAILS

In this study, we have considered three glass-forming systems: pure silica ( $\text{SiO}_2$ ) and two binary sodasilicates,  $\text{Na}_2\text{O}-5\text{SiO}_2$  and  $\text{Na}_2\text{O}-3\text{SiO}_2$ , denoted hereafter as NS5 and NS3, respectively. To start, we prepared a bulk-liquid sample

containing around 400 atoms randomly placed in a cubic simulation box and carried out classical molecular dynamics simulations at relatively high temperatures (3600 K for  $\text{SiO}_2$  and at 3000 K for the two sodasilicates), using periodic boundary conditions. The initial box side was chosen so that the density coincides with that of the glass of the corresponding composition at room temperature [47]. More details can be found in Ref. [48]. The final configurations of these classical simulations were then used as starting points for the equilibration runs carried out within the framework of *ab initio* molecular dynamics (AIMD) simulations at the same temperatures and using the constant volume–constant temperature (*NVT*) ensemble. The lengths of these AIMD trajectories were 12.2, 15.6, and 11.8 ps for silica, NS5, and NS3, respectively, a time span that was sufficiently long to completely equilibrate the samples. More details (composition, number of atoms, densities, box sizes of bulk samples) are given in Table I. For each composition, two independent samples were prepared and the results presented in the following sections are their averaged properties.

In order to generate samples that have surfaces, we cleaved the bulk-liquid samples along the  $z$  axis and inserted a vacuum layer between the two surfaces, thus creating a sample with a slab geometry. The height of this vacuum layer was 18 Å, large enough to prevent the two surfaces to interact with each other. Due to the cleavage process the structure close to the surfaces was strongly out of equilibrium and, hence, we reequilibrated the sample at a temperature  $T_0$  (see Table I). Note that the presence of the free surfaces requires that this equilibration is done with some caution: On one hand, the temperature should be high enough to allow the atoms to diffuse within a reasonable amount of time. On the other hand, a temperature that is too high will result in a substantial expansion of the sample so that the two surfaces will connect to each other. (Note that for *ab initio* simulations that use a plane-wave basis the increase of the empty space would result in additional computational cost). In addition, a high temperature might result in a partial evaporation of the Na atoms into the empty space, which can turn out into a change in the composition of the samples. For this reason, the equilibration temperature  $T_0$  for silica and the NS5 samples was identical to the one at which the liquid was equilibrated since the expansion is small, while for the Na-rich composition NS3, for which the higher network depolymerization results in a larger expansion, we had to choose a lower temperature, namely, 2200 K.

The time for equilibration at  $T_0$  was around 12 ps, which is long enough for the structure to relax. The samples were subsequently quenched down to an intermediate temperature  $T_1$  using a nominal cooling rate of  $5 \times 10^{14}$  K/s, and then to 300 K using a faster cooling rate of  $2 \times 10^{15}$  K/s. The temperature  $T_1$  was 2500, 2000, and 1500 K for silica, NS5, and NS3, respectively, values that were chosen such they are below the glass transition temperature  $T_g$  of the simulated glasses which, due to the fast cooling rates, are above the experimental  $T_g$ 's. Finally, the samples were annealed at room temperature for another 3 ps. All simulations were carried out using the *NVT* ensemble. For the calculation and analysis of the observables of interest, we discarded the first 4 ps from the total length of the runs at  $T_0$ , and 0.5 ps at 300 K. Finally, the samples were quenched to 0 K and relaxed, and then we

TABLE I. Simulation parameters. See the main text for the definitions of  $T_0$  and  $T_1$ .

No. of atoms	Na <sub>2</sub> O-mole%	$L_{\text{bulk}}$ (Å)	$\rho_{\text{bulk}}$ (g/cm <sup>3</sup> )	$T_0$ (K)	$T_1$ (K)
SiO <sub>2</sub>	384	0.0	17.96	2.20	3600
NS5	414	16.7	18.07	2.35	3000
NS3	396	25.0	17.62	2.43	2200

calculated the dynamical matrix and the Born charge tensors in order to compute the vibrational density of states (VDOS) as well as the imaginary part of the dielectric function. (see Ref. [49] for details).

The AIMD simulations were performed by using the Vienna *ab initio* package (VASP) [50,51] which implements the Kohn-Sham (KS) formulation of the density functional theory (DFT) [52,53] to compute the electronic structure. For the exchange and correlation term, we used the generalized gradient approximation (GGA) and the PBEsol functional, respectively [54,55]. The KS orbitals were expanded in a plane-wave basis at the  $\Gamma$  point and the electron-ion interaction was described within the projector-augmented-wave formalism [56,57]. We used a plane-wave basis set with a relatively high energy cutoff, namely,  $E_{\text{cut}} = 600$  eV. For the MD simulations, we used an incomplete basis of wave vectors for the density which reduced the computational cost while keeping the same accuracy for forces calculations. When computing the vibrational properties we switched to a plane-wave basis for the density containing wave vectors up to  $2G_{\text{cut}}$  where  $G_{\text{cut}}$  is the maximum of the wave vectors used for the orbitals ( $E_{\text{cut}} = \frac{\hbar^2}{2m_e}|G_{\text{cut}}|^2$ ). For solving the KS equations, the residual minimization method-direct inversion was used in the iterative space, and the electronic convergence criterion was fixed at  $1 \times 10^{-6}$  eV during the glass production process and at  $5 \times 10^{-7}$  eV for the geometric optimization procedure.

The time step for the simulations was 1 fs and temperature was controlled by a Nosé thermostat [58]. We note that the simulation parameters chosen here are similar to the ones of previous *ab initio* studies of silicate liquids and glasses in the bulk [49,59–61], and which have demonstrated that the resulting properties of the liquid and glass compare very well with experimental results.

### III. STRUCTURE

In this section we describe how to identify the surface and interior domains of our samples, called hereafter “sandwich samples” since along the  $z$  axis we have the interior (bulklike) region sandwiched between two (top and bottom) surface layers. Subsequently, we will characterize their atomic structure in terms of pair and bond-angle distribution functions as well as the concentration of the various species and local environments. These features will then be discussed with respect to both their compositional dependence and location in the two subdomains, i.e., surface and interior.

#### A. Defining the surface domain

Figure 1 shows snapshots of the simulation boxes of the glasses for the three compositions at 300 K. One sees that

the slab has an atomic disordered network structure which becomes increasingly depolymerized with the addition of Na<sub>2</sub>O. In Fig. 2 we plot the density and atomic concentrations for the liquid state ( $T = T_0$ ) as a function of the  $z$  coordinate, i.e., perpendicular to the surface. (Note that in the  $z$  direction the center of mass of the sample is defined to be at  $z = 0$ ). For all three compositions the total density distributions show a relatively flat region for  $|z| \leq 6$  Å, with densities around 2.2 g/cm<sup>3</sup> (silica), 2.3 g/cm<sup>3</sup> (NS5), and 2.4 g/cm<sup>3</sup> (NS3) [Figs. 2(a)–2(c)]. However, as we will discuss below, although these values are similar to the bulk densities, reported in Table I, this similarity does not imply that the inner region of the sandwich sample presents the same properties as a real bulk glass.

Also included in Fig. 2(b) are the density distributions for the NS5 glass at 300 K (dashed lines). Within the available statistics we do not find significant differences between the distributions for the liquid and the ones for the glass, except for the fact that the latter are slightly narrower due to the shrinking of the sample during the cooling process, resulting in a density of the interior part which is slightly higher than that of the liquid. These observations hold for all three compositions. This fact allows us to use in the following a simple criterion for defining the different domains for both liquids and glasses: Atoms having a  $z$  coordinate with  $|z| \leq 6$  Å will be defined to belong to the interior part of the sample, while atoms with a  $z$  coordinate beyond this threshold are defined to belong to the surface layers. A similar strategy for defining surfaces was also used in previous simulation studies of glass surfaces (see, for examples, Refs. [35,36,41,43]).

Figures 2(d)–2(f) depict the profiles of the atomic-number fraction along the  $z$  direction. For silica, we find that the concentration of oxygens in the surface regions is higher than in the interior layer, indicating that the top 2 Å of the surface layers are enriched in O, fall slightly below the bulk value at around 3–4 Å, and, after a small secondary peak, attains the bulk value, observations that are in agreement with previous classical and *ab initio* simulations of silica surface [22,31,35,41]. For the sodium silicate glasses, i.e., NS5 and NS3, the surface layers are strongly enriched in Na and consequently the fractions of Si and O decrease. This Na enrichment reaches about a factor of 3 (5) with respect to the bulk value of NS5 and NS3, respectively. For the NS3 surface the Na fraction reaches in fact 100%, i.e., the whole outermost layer is composed by pure Na. These findings are consistent with experimental observations of the surfaces of alkali silicate glasses by using LEIS spectroscopy [10–12] as well as with recent findings from classical molecular simulations of sodosilicate glasses with reactive force fields [62].

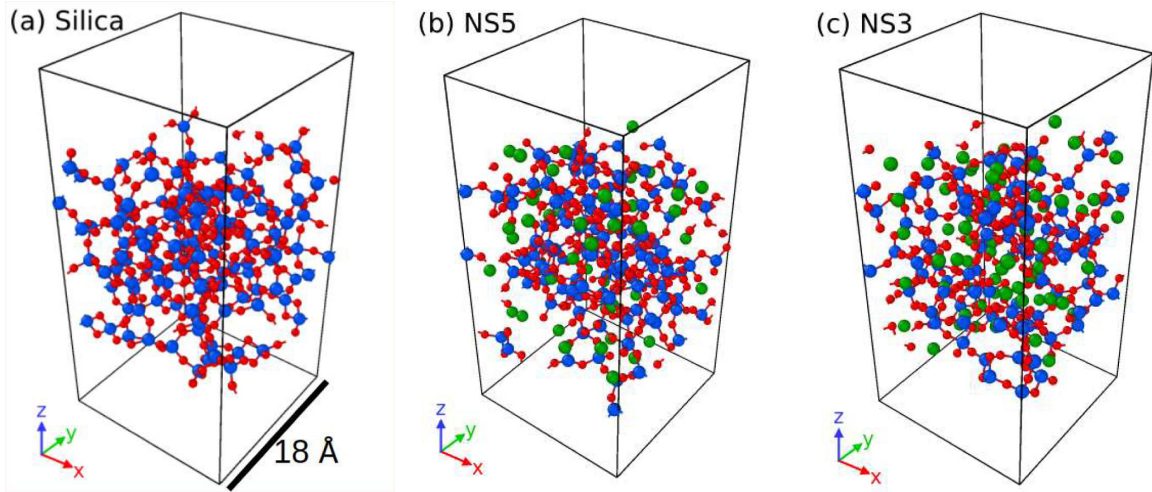


FIG. 1. Snapshots of the atomic structure of the three glasses at 300 K. Si, O, and Na atoms are represented by spheres in blue, red, and green, respectively. The sticks represent Si-O bonds with bond length smaller than 2 Å.

### B. Bond lengths and angles

Further insight into the structure of the glass surfaces can be obtained by investigating the interatomic distances, bond angles, and by the identification of the main local structural motifs. To start, we show in Fig. 3 the (normalized) probability distribution function (PDF) of the nearest-neighbor distances for the Si-O and Si-Si pairs calculated for the interior and surface regions. For the Si-O pair [Figs. 3(a)–3(c)], we clearly see that the distribution for the surfaces shifts to larger dis-

tances with respect to the interior ones. In addition, the Si-O PDFs are broader for the surface domains of NS5 and NS3 systems, which reflects the increase of the network depolymerization and disorder with respect to the corresponding properties in the interior. As we will see below, in the surface domain the fraction of nonbridging oxygens (NBO) is indeed enhanced with respect to the interior, while the fraction of bridging oxygens (BO) is smaller. (Note that the BO atoms are oxygen atoms bonded to two silicones, while NBOs connect

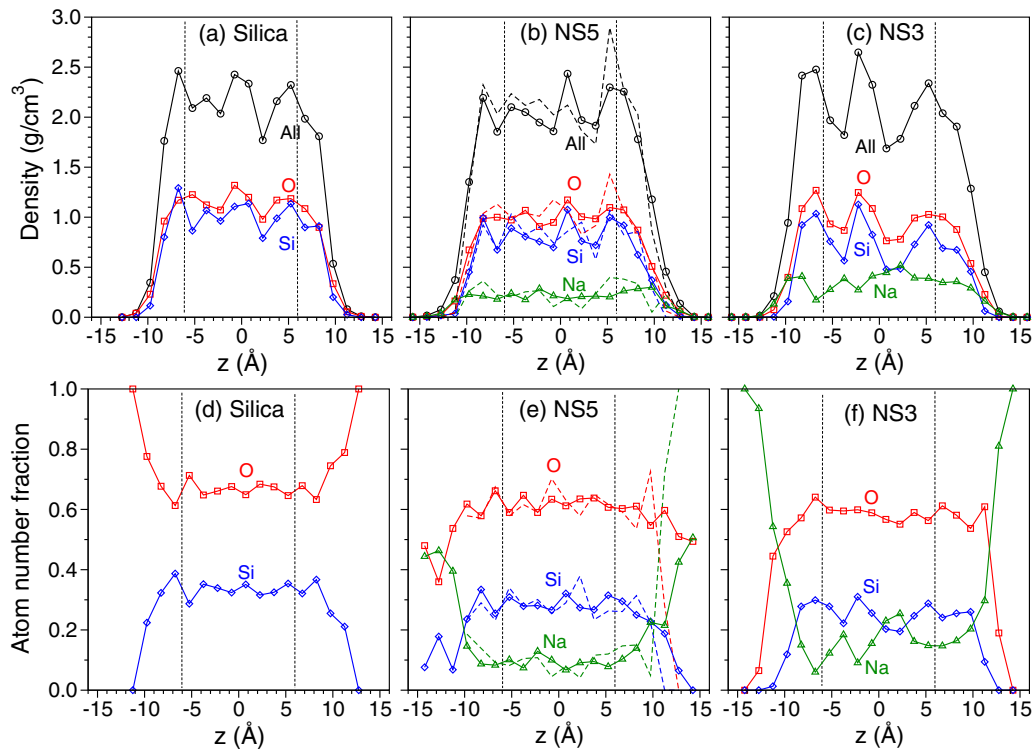


FIG. 2. Atomic distribution along the  $z$  direction. (a)–(c) The mass density profiles for silica, NS5, and NS3. (d)–(f) The atomic-number fraction along the  $z$  direction for silica, NS5, and NS3. In all graphs, the solid lines with symbols are for the liquids at temperature  $T_0$  (see Table I). The dashed lines are the corresponding quantities for glasses at 300 K and for clarity are shown only for NS5. The vertical dashed lines indicate the boundary between the surface and interior layers.

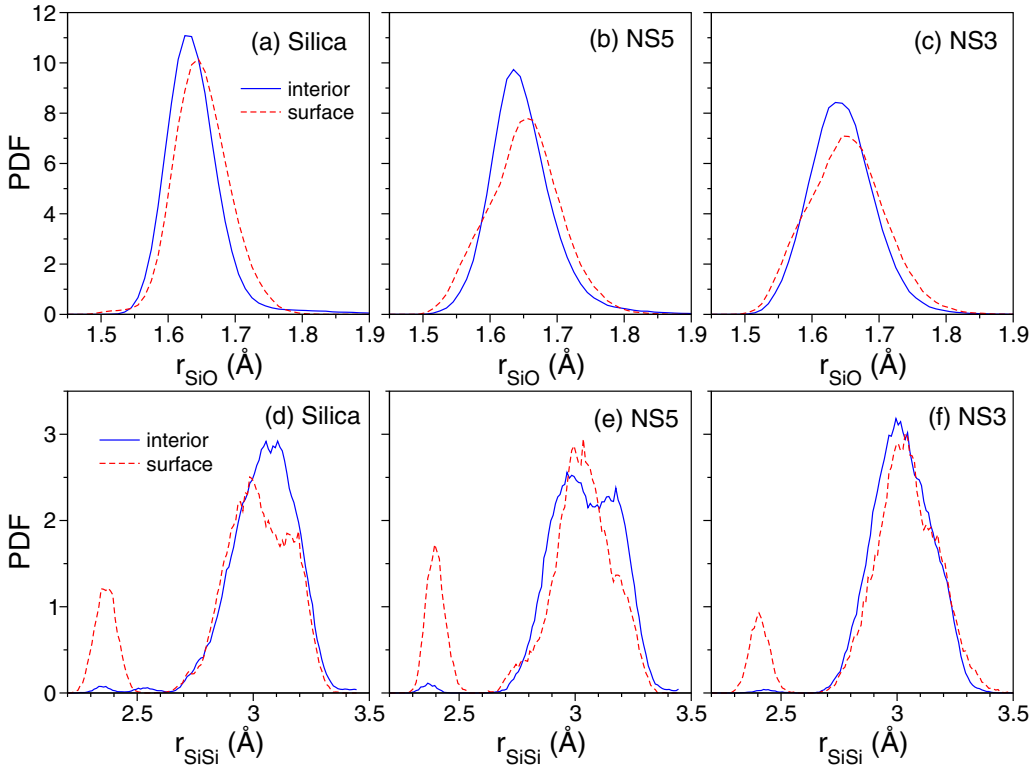


FIG. 3. Probability distribution function of nearest-neighbor distance for the glasses at 300 K. Upper and lower panels are for Si-O and Si-Si pairs, respectively. From left to right the compositions are silica, NS5, and NS3, the solid lines being for the surface domains, while the dashed lines for the interior ones.

to only one silicon.) For the Si-Si pair [Figs. 3(d)–3(f)], a prominent feature is the peak at around 2.4 Å, in particular for the surfaces. This length corresponds to the Si-Si first-neighbor distances between two tetrahedra that share an edge and thus form a two-membered (2M) ring, a structural defect often found on dehydroxylated and dry surface of silica glass [23–26,63–65]. Hence, our results show that such structures are not only present at the surface of silica, but also in the sodosilicate systems.

TABLE II. Average bond lengths for the sandwich glass samples at 300 K for both surface and interior domains. csSi and esSi denote, respectively, corner-sharing and edge-sharing Si.

Glass Bond	Silica Int. (Å)/surf. (Å)	NS5 Int. (Å)/surf. (Å)	NS3 Int. (Å)/surf. (Å)
Si-Si	3.041/2.928	3.041/2.927	3.021/2.986
csSi-csSi	3.048/3.006	3.041/3.059	3.023/3.024
csSi-esSi	3.055/3.058	3.189/3.000	2.956/3.108
esSi-esSi	2.443/2.483	2.370/2.408	2.437/2.408
Si-O	1.638/1.650	1.648/1.651	1.645/1.651
Si-NBO	–/1.563	1.578/1.576	1.588/1.585
Si-BO	1.638/1.652	1.652/1.664	1.655/1.670
esSi-esBO	1.721/1.684	1.678/1.695	1.704/1.695
Na-O		2.423/2.362	2.423/2.375
Na-NBO		2.276/2.264	2.347/2.315
Na-BO		2.526/2.531	2.545/2.494

In Table II, we report the average first-neighbor distances for the Si-O, Si-Si, and Na-O pairs, as well as the ones related to 2M rings. The bond lengths with respect to oxygens are further decomposed with respect to the two species BO and NBO. For both domains, we see that the distances Si-NBO and Na-NBO are significantly shorter than the Si-BO and Na-BO distances, as already pointed out in simulations for bulk systems and in agreement with experimental findings [49,66–69]. For the sodosilicates we find that the average Na-O distances in the surface domains are shorter than the ones in the interior as a consequence of the Na enrichment of the surface domains [see Figs. 2(e) and 2(f)], which leads to the increased fraction of NBOs and thus making the network less polymerized and hence with less constraints compared to the interior part. The same trend has also been found in a recent study of the surface structure of sodium silicates glasses using classical MD [9].

In silicate glasses, the Si-Si first-neighbor distance is a measure of the intertetrahedral distance between two corner-sharing (cs) tetrahedra, with typical values around 3.00–3.08 Å [70]. This range is compatible with the values we find in the interior domain of our three glasses, while for the surface domains this distance is shorter by 2%–3% (see Table II). A further decomposition of the structure into local motifs shows that this reduction in the Si-Si distance for the surfaces is due to the presence of edge-sharing (es) tetrahedra forming the 2M rings mentioned above. The 2M rings found in our samples have tetrahedra that are strained, characterized by short Si-Si distances, elongated Si-O bonds, and reduced Si-O-Si and OSiO angles (see below). As a

TABLE III. Percentages of various atomic species in the interior and surface domains for the silica and sodosilicate samples. Liquids correspond to simulation at  $T_0$  (see Table I), and glasses are at 300 K. On the first row,  $N_{\text{domain}}$  denotes the percentage of atoms in a specific domain with respect to the total number of atoms of the sample. The proportions of the atomic species are given relative to their concentration in the considered domain. Note that, for the surface domain, we give the sum of the amounts on the top and bottom surface layers.

% $N_{\text{domain}}$	Silica		NS5		NS3	
	Liquid Int./surf.	Glass Int./surf.	Liquid Int./surf.	Glass Int./surf.	Liquid Int./surf.	Glass Int./surf.
$N_{\text{domain}}$	65.8/34.2	66.7/33.3	58.6/41.4	60.7/39.3	58.5/41.5	62.9/37.1
Si	33.2/33.7	33.3/33.4	29.1/26.0	29.1/25.7	25.5/24.4	25.8/23.7
O	66.8/66.3	66.7/66.6	61.9/60.0	62/59.7	58.3/58.4	58.3/58.4
Na	0/0	0/0	9.1/14.0	8.9/14.6	16.3/17.2	15.9/17.9
$\text{Si}^3$	2.3/3.7	0/1.6	0.7/1.7	0/0	0.1/0.8	0/0
$\text{Si}^4$	29.6/28.8	32.9/31.8	27.2/23.6	27.5/25.7	24.3/23.3	25.4/23.7
$\text{Si}^5$	1.2/0.8	0.4/0	1.2/0.6	1.6/0	1.1/0.3	0.4/0
NBO	2.4/4.6	0/2.3	8.1/16.7	6.6/15.6	14.3/19.7	14.9/19
BO	64.4/61.7	66.7/64.3	53.8/43.3	55.4/44.1	43.9/38.7	43.5/39.3
esBO	4.9/11.1	1.4/12.8	3.4/7.5	1.6/9.8	1.8/4	0.8/4.1
esSi	4.6/11.3	1.6/12.5	3.3/7.1	1.2/10.5	1.6/4.1	0.4/4.8

consequence, the esSi-esSi distance gives rise to an additional peak seen in Figs. 3(d)–3(f) located around 2.4 Å (see also Table II).

Table II shows that in our sandwich samples the esSi-esSi distance is close to 2.4 Å and, within the accuracy of our data, independent of the composition and whether the atoms are located in the surface or in the interior domain, values that compare well with results obtained from previous classical MD simulations [31,32,35,36,38,41], showing that this distance is not very dependent on the potential used for the simulations. The 2M rings found in our samples are also characterized by Si-O bonds that are stretched with respect to those in corner-sharing tetrahedra, and the values reported in Table II are in good agreement with those found in classical MD simulations [31,32,38] as well as in a recent AIMD investigation of dehydroxylated silica surfaces [71]. This elongation of the bond is also compatible with DFT calculations of crystalline fibrous silica containing chains of 2M rings [72] as well as Hartree-Fock calculations of clusters and molecules containing 2M rings [25,73] which found esSi-esBO bond lengths around 1.67 Å and esSi-esSi distances between 2.38–2.42 Å. Finally, we mention that the presence of elongated esSi-esBO bonds together with small Si-O-Si angles as structural fingerprints of 2M rings is also consistent with the findings from a recent DFT study considering the surfaces of  $\beta$ -cristobalite [74]. As a consequence, we conclude that (i) for silica the geometrical properties of our 2M rings are compatible with previous results and (ii) the geometry of these rings are basically independent of the environment of the ring.

In order to characterize the structure of our sandwich systems in a more quantitative manner, we have determined the fractions of various atomic species present in the interior and surface domains, and the data are summarized in Table III. One recognizes that for the sodosilicate systems the surface domains are enriched in sodium, in agreement with the atomic distribution along the  $z$  axis, shown in Figs. 2(d)–2(f). For NS5 this enrichment is about 50% while for NS3 it is still

around 10%, independent whether one considers the liquid or the glass state. Furthermore, we have decomposed in both domains the concentration of the silicon and oxygen atoms with respect to their coordination numbers. (For this we used a cutoff distance of 2.0 Å to define bonded pairs). We find that most Si atoms are fourfold coordinated but also note the presence of undercoordinated and overcoordinated atoms,  $\text{Si}^3$  and  $\text{Si}^5$ , respectively. For the systems with sodium we see that in the liquid state there is a small concentration of fivefold coordinated Si for both surface and interior domains but that during the quench these defects disappear in the surface domains, while a very small number are still present in the interior domains, possibly as a consequence of the high quench rate [59]. For the threefold Si we note that in the liquid state they are more concentrated in the surface layers than in the interiors and that in the glassy state they are absent for the sodium silicate systems

From the data reported in Table III one also recognizes that the surface domains have a significantly higher concentration of NBOs than the interior. With increasing  $\text{Na}_2\text{O}$  content, the concentration of surface NBO increases, and this may account for the reduction of both undercoordinated and overcoordinated silicons since with increasing Na content more NBO are formed, allowing the Si atoms to grab/shed O atoms and hence to form a more regular local environment, i.e., becoming fourfold coordinated.

The last two rows in Table III give the percentages of the silicon and oxygen atoms that form 2M rings (labeled esSi and esBO, respectively). As expected, these rings are more abundant on the surface than in the interior, by a factor of around 2 in the liquid state and a factor 5–8 in the glass samples. This temperature dependence is mainly due to the  $T$  dependence of the concentration of the 2M rings in the interior since on the surface this concentration is basically independent of  $T$ . This indicates that these structures are energetically very unfavorable in the bulk while they are a energetically reasonable building block in the presence of a free surface.

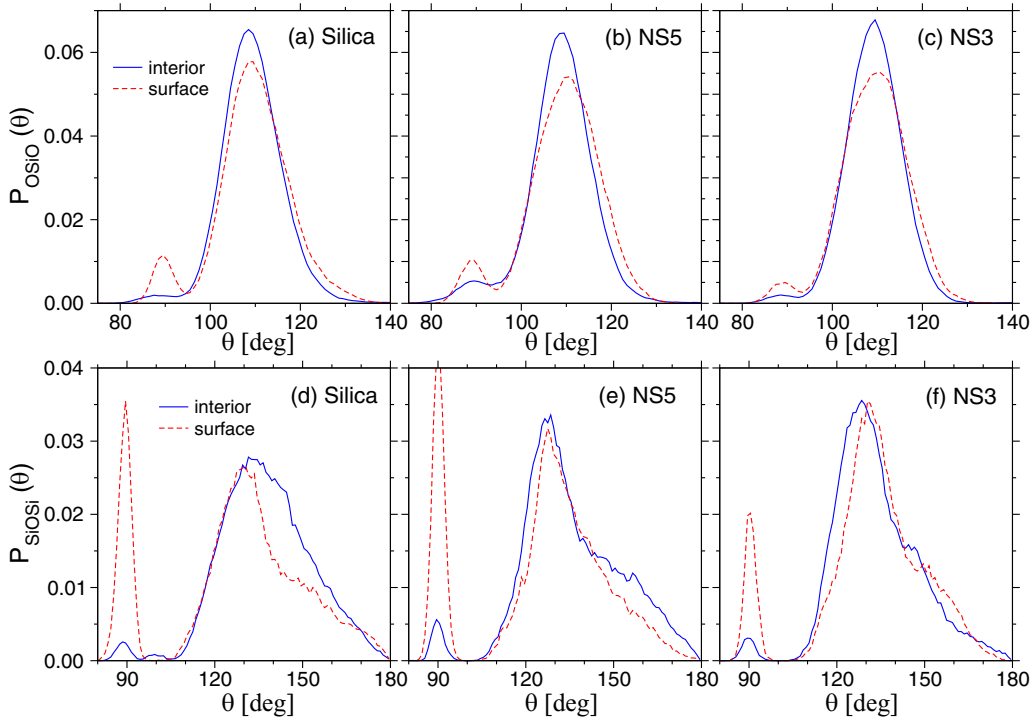


FIG. 4. Bond-angle distribution. Upper and lower panels are for O-Si-O and Si-O-Si angles, respectively. From left to right the compositions are silica, NS5, and NS3.

From the numbers of 2M rings we can calculate their area density by dividing this number by the surface area. For silica, we find a density of  $1.5/\text{nm}^2$  which has to be compared with the estimate obtained from IR experiments which give values of 0.2 to  $0.4/\text{nm}^2$ . (As discussed below, 2M rings have a spectroscopic signature in the absorption IR spectrum, with two peaks at  $888$  and  $908 \text{ cm}^{-1}$  and a weak shoulder at  $932 \text{ cm}^{-1}$  [24–26,29,75]). Also, previous simulation studies on dry silica have reported smaller densities of 2M rings and this might be rationalized by the fact that most of these simulations were carried out using classical MD approaches, thus allowing for quench rates that are considerably lower than the one used in this study [36,41]. To our knowledge, the models of silica surface labeled as *ab initio* in the literature were initially prepared by melting and quenching a liquid silica using effective, i.e., classical, potentials and the obtained structure was processed within a first-principles framework only at 300 K (see, for example, Ref. [22] and references therein). The present samples are hence the first ones generated by the quench of a liquid surface within an AIMD approach, admittedly with a very high quench rate which prevents the annealing and relaxation of the glass surface.

More insight into the structural differences between the surface and interior domains and the compositional effect can be obtained by computing the bond-angle distributions (BAD) shown in Fig. 4 for the glass samples. The main peak in the BAD for O-Si-O is located at around  $109^\circ$ , the expected angle for a perfect tetrahedron [Figs. 4(a)–4(c)]. One also notices that the distribution of surface O-Si-O angle is slightly wider than the interior, which indicates that the  $[\text{SiO}_n]$  units on the surface are more distorted than the interior ones. For pure silica, we see that the main peak of the Si-O-Si BAD ( $>100^\circ$ )

[Fig. 4(d)] is narrower and more asymmetric for the surface domain. The peak at around  $130^\circ$  is similar to the one found in the NS5 and NS3 systems [Figs. 4(e) and 4(f)], i.e., the glasses that are more depolymerized. For the NS5 system [Fig. 4(e)], the mentioned asymmetry is still present but less pronounced, while for the Na-rich glass it has basically disappeared due to the presence of Na atoms. For the interior domains, the main peak becomes sharper and shifts to smaller angle with the addition of  $\text{Na}_2\text{O}$ , a trend pointed out also in a previous *ab initio* study of bulk sodium silicate glasses [69].

For both the O-Si-O and Si-O-Si BADs, we observe a peak at around  $90^\circ$ , which is due to the 2M rings. This peak is more pronounced for the surfaces, which is consistent with the structural data discussed above, i.e., the presence of small Si-Si distances and a significant fraction of the esSi and esBO in the surface domains. The location of these peaks is in qualitative agreement with earlier MD simulations with classical potentials [31,32,36,38,41], and also the aforementioned DFT [72] and molecular orbital calculations [25,73] obtained optimized structures of edge-sharing tetrahedra with similar highly distorted Si-O-Si angles around  $90^\circ$ .

In order to visualize some of the above-mentioned structural features of the surfaces and their compositional differences, we show in Fig. 5 snapshots corresponding to the outermost atoms of the surface domains of silica and NS3 glasses. In order to select the atoms shown in Fig. 5, we have first identified the Si atoms belonging to the surface using the tetrahedralization-based method proposed by Edelsbrunner and Mücke [76]. The probing sphere radius used for this algorithm was chosen as  $3.2 \text{ \AA}$ , i.e., around the nearest-neighbor distances of Si-Si (see Refs. [9,48] for details). The first-nearest O and Na neighbors of these surface silicons have

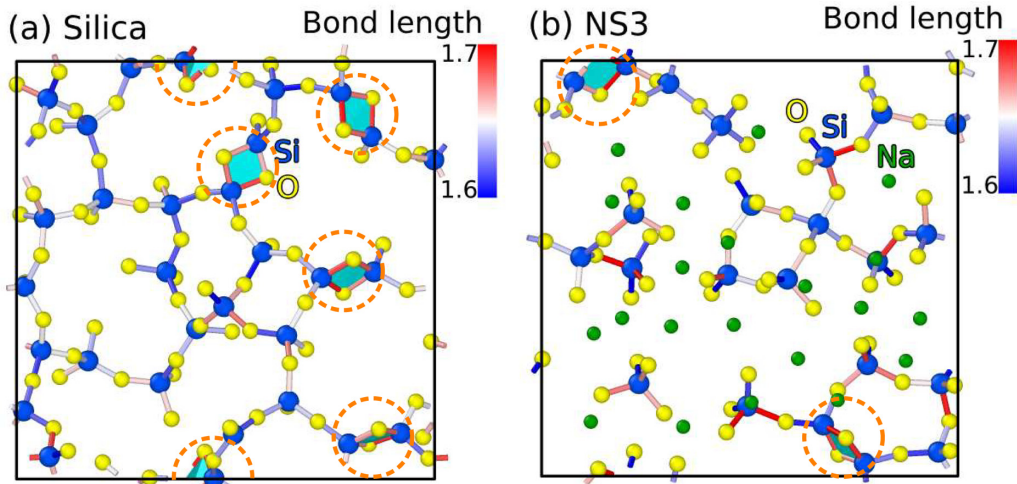


FIG. 5. Top view of snapshots showing structural motifs at the surfaces of (a) silica and (b) NS3 glasses. Only the outermost layer of silicon atoms and their nearest-neighbor O and Na atoms are shown (see the text for the construction method). Two-membered rings are highlighted with a circle. Only Si-O bonds are shown and a color code is used taking into account their length, given in Å. The visualization was realized using OVITO [77].

then been found and included in the snapshots, whereas the other atoms have been removed from the sake of clarity. For silica [Fig. 5(a)], 2- to 9-M rings are found on the surface. With the addition of sodium, the network of the atomic surface layer of the NS3 glass [Fig. 5(b)] becomes less connected, and the proportion of 2M rings is decreased: While for silica we observe five 2M rings, only two are found for NS3. As argued above, this difference in concentration is likely due to the fact that 2M rings are strongly strained, with smaller Si-O-Si bond angles and longer Si-O bond lengths with respect to the typical values (see bond color code in Fig. 5). The presence of Na can effectively relieve surface tension by breaking some of these Si-O bonds (notably in small rings) and thus make the surface energetically more stable.

### C. Orientational analysis

In the previous subsections we have discussed the geometrical properties of the local structural units, mainly tetrahedra, in terms of bond angles and lengths. In the following we probe the orientation of these tetrahedra with respect to the surface. As a parameter describing the orientation of a tetrahedron, we used the angle  $\theta$  between a unit vector along a SiO bond pointing toward the oxygen,  $\hat{\mathbf{u}}_{\text{SiO}}$ , and a unit vector  $\hat{\mathbf{u}}_{\text{surface}}$  along the  $z$  axis (i.e., perpendicular to the surface) oriented from the interior domain toward the closest surface. The inset of Fig. 6(b) illustrates schematically this definition. Note that in the snapshot only three oxygen atoms are visible as the fourth one is superimposed with the bottom oxygen on the right hand side. Among the four bonds of a tetrahedron we chose the one that is most aligned with respect to the  $z$  direction, i.e., the one for which  $|\sin \theta|$  has the smallest value. Note that  $\theta = 0^\circ$  and  $180^\circ$  indicate that the tetrahedron is perfectly perpendicular to the surface but oriented in opposite directions.

In Fig. 6 we show the distributions of the angle  $\theta$  for the liquid samples. We also included the distribution (black dashed lines) obtained for the case that the tetrahedra are oriented randomly, and this will serve us as a reference distri-

bution. For all samples, as well as the random distribution, we observe two pronounced peaks, at around  $30^\circ$  and  $150^\circ$ , which correspond to the most likely direction due to phase-space arguments. For the interior part of the samples we see that the measured distribution is very close to the random one, demonstrating that from the point of view of the orientations of the tetrahedra the interior is only mildly affected by the presence of the surfaces. In contrast to this, we observe for the surface domain in liquid silica [Fig. 6(a)] that the peak at  $30^\circ$  shifts to larger angles and becomes broader, while the one at  $150^\circ$  shifts slightly to smaller angles and its intensity increases. This indicates that the tetrahedra close to the surface attempt to orient such that three of the oxygens are close to the surface, in agreement with the observation from Fig. 2(d) that the surface has a higher concentration of oxygen than the bulk. For the samples with Na, we see only a marginal difference between the distributions of  $\theta$  for the interior and the one for the surface [Figs. 6(b) and 6(c)]. This result is reasonable since the pronounced presence of sodium at the surface makes that the oxygen atoms have no reason to try to get close to the surface (see Fig. 2), and hence the orientation of the tetrahedra stays close to random. Finally, we mention that the trends inferred from the liquid samples shown in Fig. 6 are compatible with the ones for the samples in the glass state, but due to the lack of statistics for this case we cannot draw strong conclusions.

## IV. VIBRATIONAL PROPERTIES

### A. Vibrational density of states

In this section we will discuss the vibrational properties of our systems in terms of the total as well as partial vibrational density of states (VDOS). After having relaxed at 0 K, we have determined and diagonalized the dynamical matrix from which one can obtain the total VDOS as

$$g(\omega) = \frac{1}{3N-3} \sum_{p=4}^{3N} \delta(\omega - \omega_p), \quad (1)$$

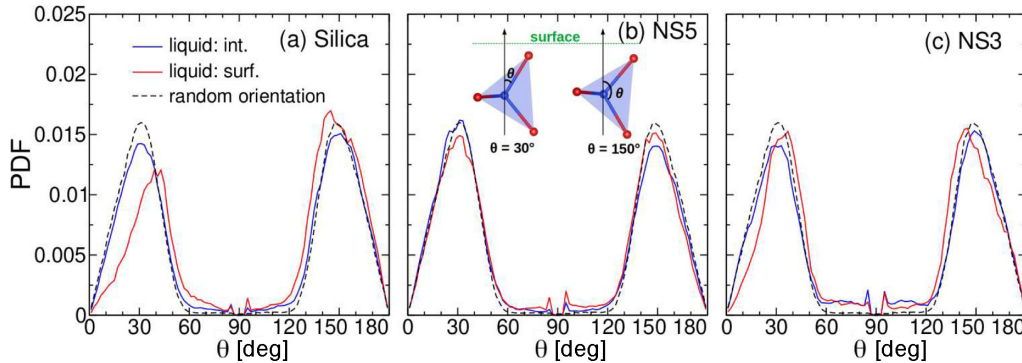


FIG. 6. Probability distribution functions of the orientation angle for the surface (red line) and interior (blue line) domains in the liquid state (at  $T_0$ ). Panels (a), (b), and (c) are for liquid silica, NS5, and NS3 composition, respectively. The black dashed lines correspond to a random orientation. The inset in (b) illustrates the tetrahedral orientations corresponding to  $\theta = 30^\circ$  and  $150^\circ$ , respectively.

where  $N$  is the total number of atoms in the sample,  $\omega$  is the frequency, and  $\omega_p$  is one of the  $3N$  eigenvalues of the dynamical matrix. This total VDOS can be decomposed further into the contributions from different species, allowing to define the partial VDOS

$$g_\alpha(\omega) = \frac{1}{3N - 3} \sum_{p=4}^{3N} \sum_{I=1}^{N_\alpha} \sum_{k=1}^3 |\mathbf{e}_{I,k}(\omega_p)|^2 \delta(\omega - \omega_p). \quad (2)$$

Here,  $\alpha \in \{\text{Si, O, Na, BO, NBO, csSi, esSi, csBO, esBO}\}$ ,  $N_\alpha$  is the number of particles of type  $\alpha$ , and  $\mathbf{e}_{I,k}(\omega_p)$  is the part of the  $3N$ -component eigenvector  $\mathbf{e}(\omega_p)$  that contains the three components of the particle  $I$ . [Note that in Eqs. (1) and (2) we do not consider the three trivial translational modes of the system]. All vibrational spectra that will be discussed in the following have been obtained by convoluting the discrete distribution given by Eq. (2) with a Gaussian function with a full width at half-maximum of  $30 \text{ cm}^{-1}$  and averaged over two independent samples.

The total VDOS of the silica and NS3 systems are shown in Fig. 7(a), alongside the partial contributions of their constituent atoms  $\alpha \in \{\text{Si, O, Na}\}$  [Figs. 7(b)–7(d)]. We recognize that each of these distributions have three main bands: A low-frequency band with  $\omega < 500 \text{ cm}^{-1}$ , a mid-frequency band with  $500 < \omega < 900 \text{ cm}^{-1}$ , and a high-frequency band with  $\omega > 900 \text{ cm}^{-1}$ . In order to recognize the influence of the surface on the spectra, we have included in Fig. 7(a) also the total VDOS of a bulk silica glass sample which was obtained from *ab initio* calculations within a framework that was similar to that used in this work [60]. The presence of the surfaces makes that all the sharp peaks observed in the bulk glass at around  $400$ ,  $800$ , and  $1000 \text{ cm}^{-1}$  are significantly smeared out and that the high-frequency band is shifted to somewhat lower frequencies, making that the gap between the mid- and high-frequency band is partially filled up. In addition, one recognizes that due to the surface the double-peak structure of the high-frequency band is completely washed out. The addition of  $\text{Na}_2\text{O}$  makes that the height of the peaks at  $400$  and

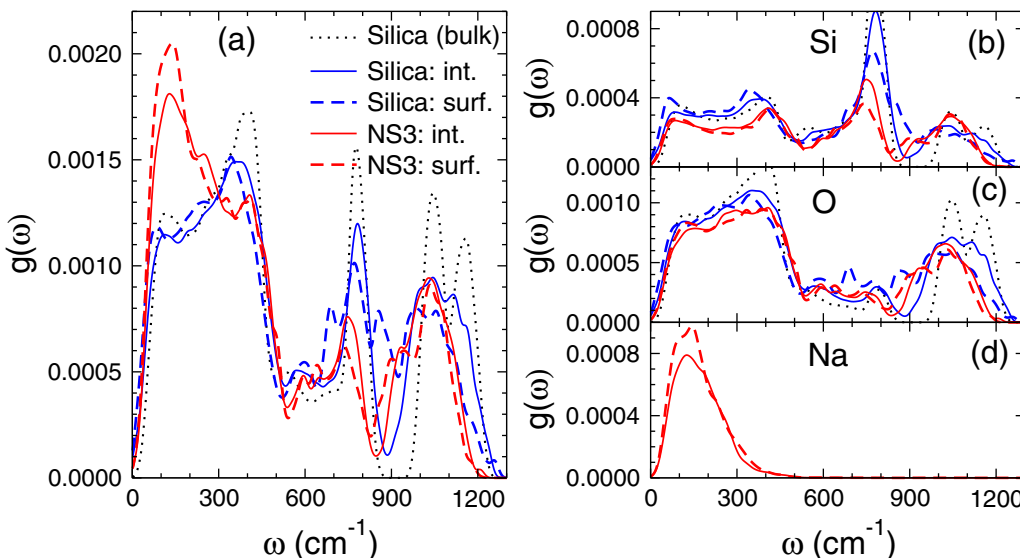


FIG. 7. (a) Total vibrational density of states (VDOS) of the two sandwich glasses at 0 K for the interior and the surface domains. (b)–(d) show the partial VDOS for the Si, O, and Na atoms, respectively. Also included in (a) is the total VDOS for a bulk silica glass from *ab initio* calculations [60]. The total VDOS in (a) are normalized to unity, which is equal to the sum of the partials as depicted in (b)–(d).

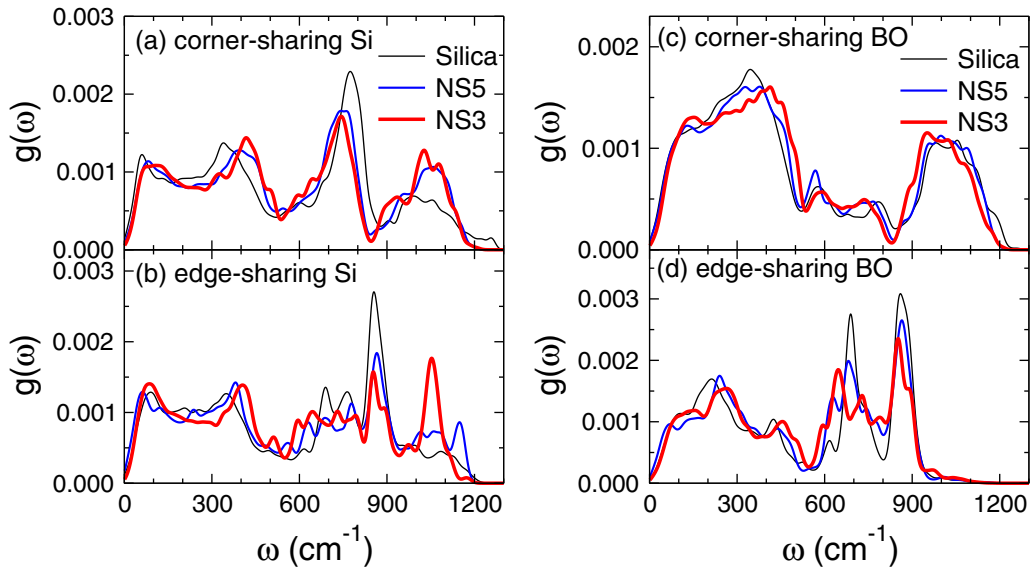


FIG. 8. Per-atom VDOS of the surface atoms. Panels (a) and (b) are for corner-sharing and edge-sharing Si atoms, respectively. Panels (c) and (d) are for corner-sharing and edge-sharing BO, respectively. All curves are normalized to unity.

$800\text{ cm}^{-1}$  decreases further while the high-frequency band is not modified in a significant manner, although it does shift to lower  $\omega$ . As it has been shown before, this softening is due to the depolymerization of the network which increases the contribution from NBO-related motions [69,78]. Finally, we note that the shape of the low-frequency band changes strongly in that a new peak at around  $150\text{ cm}^{-1}$  starts to grow with increasing Na concentration, a feature that is also seen in spectra of bulk sodiosilicate glasses [69].

A better understanding of these changes can be obtained by inspecting the partial VDOS, presented in Figs. 7(b)–7(d). [Note that the sum of the three partials gives the total VDOS shown in Fig. 7(a)]. It is clearly seen from Fig. 7(b) that the band at around  $800\text{ cm}^{-1}$  is related to the vibrational motion of Si, in agreement with earlier studies which have shown that the peak is related to the complex motion of Si against BO [78]. The decrease of the peak height with the addition of Na can thus be expected to be related to the (partial) breaking up of the network, i.e., the decreasing number of BO. Figure 7(c) shows that oxygen is the dominant contributor to the spectrum in the low-frequency band and that also in the high-frequency band its partial VDOS is larger than the one of Si.

The experimental IR spectra for silica surfaces show two strong peaks at  $888$  and  $908\text{ cm}^{-1}$  and a shoulder at  $932\text{ cm}^{-1}$  [24–26,29,75]. These features have been related to the presence of 2M rings, an assignment which is supported by electronic structure calculations for small terminated 2M ring clusters [79] as well as of dehydroxylated silica surface [80]. In order to identify the vibrational signal of 2M rings in our sandwich samples, we have decomposed the partial VDOS of surface BO and Si into contributions from edge-sharing and corner-sharing atoms (Fig. 8). (We mention that to a first approximation the VDOS of the corner-sharing atoms [Figs. 8(a) and 8(c)] are the same as the spectra for the bulk. In reality, however, the presence of the surface gives rise to a slight modification of the spectra.) Figures 8(b) and 8(d) clearly show that esSi as well as esBO have a strong signal between

$800$  and  $900\text{ cm}^{-1}$ , a frequency range in which the spectra for csSi and csBO have low intensity. The main peak in this range is at around  $850\text{ cm}^{-1}$ , i.e., a frequency which is somewhat lower than the experimental window which ranges from  $888$  to  $932\text{ cm}^{-1}$ , but a value that agrees well with previous DFT calculations [80].

In addition to the vibrational features discussed above, we note in the partial VDOS for the esBO a further signature of the 2M rings in the form of a pronounced peak at around  $700\text{ cm}^{-1}$  [Fig. 8(d)]. This peak is completely absent in the spectra for the csBO and its position shifts to lower frequencies with increasing Na<sub>2</sub>O concentration. At this frequency also the partial VDOS of the csSi shows a peak, but its intensity is not very high. To the best of our knowledge, the existence of these peaks for the vibrational spectra of 2M rings has not been reported before and at present we do not know to which type of motion it corresponds.

Due to the presence of the surface one can expect that the vibrational modes are no longer isotropic and that hence also the VDOS will become anisotropic. That for the case of NS3 this is indeed the case is demonstrated in Fig. 9 where we present the partial VDOS as obtained for the three different directions:  $x$  and  $y$  parallel to the surface and  $z$  orthogonal to it. We see that the curves for the  $x$  and  $y$  directions coincide with high accuracy, indicating that the error bars are small. The spectrum for the  $z$  direction shows significant deviations from the two other curves, see arrows, notably at around  $100\text{ cm}^{-1}$ , i.e., the peak that is directly related to the vibrational motion of the Na atoms. Figure 9(c) shows that the vibrations in the  $z$  direction are a bit softer than in the two other directions (the peak is shifted to lower frequencies), a result that is reasonable since the Na atoms are less constrained in the  $z$  direction. The anisotropy can also be seen in the high-frequency band in that the intensity of the spectrum in the  $z$  direction for Si and O is lower than the one in the orthogonal directions. This result can be rationalized by the fact that close to the surface the Si-O-network is more anisotropic since we

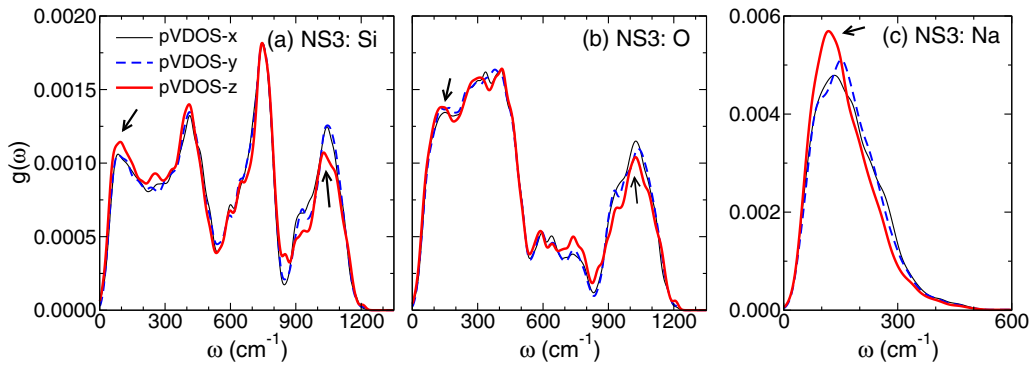


FIG. 9. Decomposition of the partial VDOS of NS3 into contributions from different directions. Panels (a)–(c) are for Si, O, and Na, respectively. The arrows indicate the locations at which the spectra depend significantly on the direction. All curves are normalized to unity.

have found (see Fig. 2) that there is a layering effect in the composition.

### B. Infrared response

In the previous subsection we have discussed the vibrational features of our sandwich systems, focusing on the frequency and composition dependencies of the partial and total VDOS. In order to make a direct connection to experimental data, it is useful to compute the IR response of the samples. This quantity can be obtained directly from the frequency dependence of the dielectric function  $\epsilon(\omega)$  which can be calculated from the vibrational eigenmodes and the Born effective charges of the atoms. (The details of the method and the relevant relations are documented in Ref. [49]). In Fig. 10 we present  $\epsilon_2(\omega)$ , the imaginary part of the dielectric function, for our three systems, for bulk silica as well as the experimental spectrum from Ref. [81]. Since  $\epsilon_2(\omega)$  has an  $\omega$  dependence which is very similar to the one of the IR absorption (see Ref. [49]), we present here the former quantity. We also recall that the IR experimental studies exhibiting the well-defined frequency window between 888 and 932 cm<sup>-1</sup> assigned to 2M rings [24–26,29,75] are absorption spectra, thus motivating this choice.

Comparing in Fig. 10(a) the theoretical spectra for the bulk with the experimental data, we see that the simulation reproduces correctly the three main resonances, although the peak positions are down-shifted by about 25–30 cm<sup>-1</sup> and the height of the peak at  $\approx 430$  cm<sup>-1</sup> is lower. These discrepancies might be due to the small size of our system or related to the fact that the DFT functional we have used in the present simulations is known to produce frequencies that are about 5% too small [82]. However, in overall the obtained agreement between the calculated  $\epsilon_2(\omega)$  and the experimental data is good and on this basis we can proceed to understand the evolution of the IR response due to the presence of the surface as well as to the composition.

Also included in Fig. 10(a) is the spectrum for the silica sandwich sample. We see that with respect to the corresponding bulk data the curve is shifted to lower frequencies by about 30 cm<sup>-1</sup> and that the three main peaks have become broader. These changes can be explained by the fact that the defective structures present in the sandwich samples (NBO, 2M rings) induce distortion of the glass network and this increased disorder leads to a softening of the vibrations and broadening of the peaks. This modification is most pronounced for the band at  $\approx 780$  cm<sup>-1</sup>, which corresponds to the symmetric stretching of the SiOSi bridges. This band not

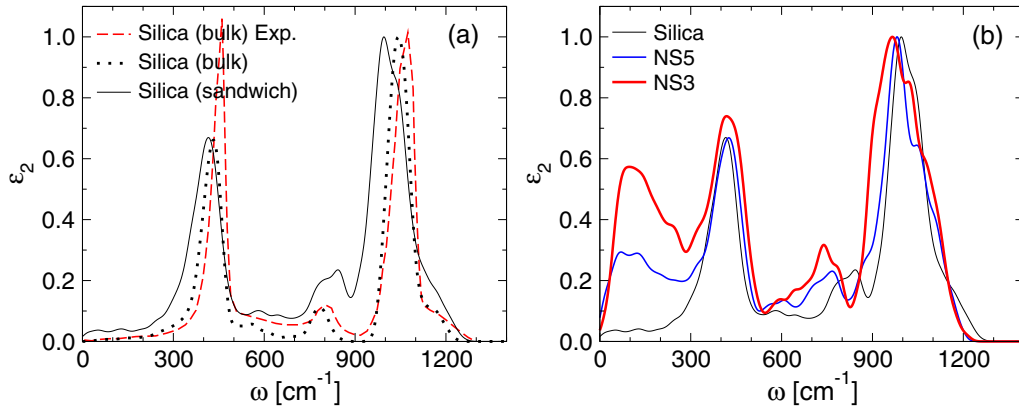


FIG. 10. Imaginary part of the dielectric function  $\epsilon_2(\omega)$  for bulk silica as well as for the three sandwich systems. (a) Shows the calculated spectra of  $\epsilon_2(\omega)$  for bulk (black dotted line) and sandwich sample (black line), and the experimental spectrum (red dashed line) for bulk amorphous silica [81]. (b) Shows the calculated  $\epsilon_2(\omega)$  for the silica, NS5, and NS3 sandwich systems, black, blue, and green full line, respectively.

only becomes broader but also asymmetric, with a new peak located close to  $850 \text{ cm}^{-1}$ , a frequency which coincides with the one of the characteristic peaks of esBO and esSi discussed in the context of Fig. 8. Thus, we can conclude that the IR spectra can indeed reveal the presence of 2M rings in the sample. However, we also note that at  $\omega \approx 700 \text{ cm}^{-1}$ , we find no marked peak in  $\epsilon_2$ , i.e., the peak we find at this frequency in the VDOS [see Fig. 8(b)] seems not to be IR active.

In order to understand the dependence of the spectrum on the composition we present in Fig. 10(b) the calculated imaginary part of the dielectric function for the three sandwich samples. First, we notice for the NS5 and NS3 glasses the presence of a broad band below  $300 \text{ cm}^{-1}$ , with an intensity that grows with the concentration of Na. This trend is in agreement with experimental IR studies for bulk glasses [83–85] and a comparison with the VDOS from Fig. 7 shows that this band is indeed directly related to the vibrational motion of the sodium atoms. In contrast to this, the pronounced peak at around  $400 \text{ cm}^{-1}$  depends only weakly on the concentration of sodium, a result due to the fact that that rocking motions of SiOSi bridges, IR active modes, are not much affected by the Na presence [69]. A stronger dependence on the Na concentration is observed for the band from  $700$  to  $900 \text{ cm}^{-1}$  in that it shifts significantly to lower frequencies, becomes more intense and slightly broader. The softening of this spectral region with the addition of Na has also been seen in experimental IR spectra for bulk glasses and attributed to the increasing depolymerization of the network, in agreement with our observations for our sandwich samples (see Sec. III). Regarding the 2M rings, we recall that their concentration decreases with increasing Na content, accompanied by a decreasing signal in the VDOS at  $\approx 850 \text{ cm}^{-1}$  (see Fig. 8). Figure 10(b) shows that at this frequency the systems with sodium do not show any sign of a peak, i.e., for such glasses IR spectroscopy experiments cannot be expected to detect the presence of 2M rings in this frequency range. Finally, we mention that in the high-frequency region the addition of Na leads to a broadening of the band and a shift of the peak to lower frequencies. These modifications are the signature of the increasing number of NBOs, and they are consistent with the changes reported in experimental works [83–85].

## V. ELECTRONIC PROPERTIES

In this section we present the electronic properties of our samples, i.e., the electronic density of states (eDOS), Bader charges, and the electron localization function (ELF). The presence of a surface in combination with the Na addition makes that these properties change significantly with respect the ones for bulk silica and we will discuss these modification in connection with the defective structures such as 2M rings or NBO.

### A. Electronic density of states

The eDOS,  $D(E)$ , can be obtained directly from the Kohn-Sham energies calculated for the structure relaxed at  $T = 0 \text{ K}$  (see Ref. [49] for details). Figure 11 shows the eDOS for the interior and surface domains of the studied compositions. For the sake of comparison, we include in Fig. 11(a) also the

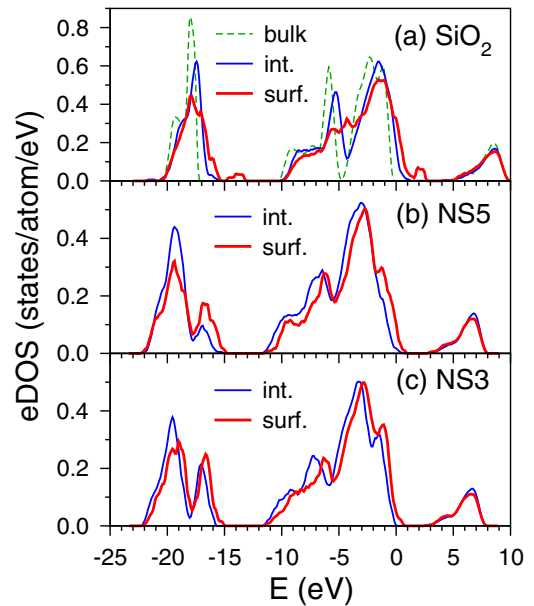


FIG. 11. Electronic density of states of the sandwich glasses at 0 K. Panels (a), (b), and (c) are for silica, NS5, and NS3, respectively. The eDOS of the sandwich glasses are decomposed with respect to the surface (surf.) and interior (int.) layers. (a) Shows also the eDOS for bulk silica. All distributions are normalized with respect to the number of atoms. The Fermi level energy  $E_f$  is at 0 eV.

data for a bulk silica glass (dashed line), computed using the same structural model as the VDOS discussed in the previous section [86]. For this bulk system we recognize features that have been documented in the literature before [87,88]: (i) The states at around  $-20 \text{ eV}$  are O 2s states; (ii) the states from  $-10$  to  $-4 \text{ eV}$  are bonding states between Si  $sp^3$  hybrids and (mainly) O 2p orbitals; (iii) the states above  $-4 \text{ eV}$  up to the Fermi level ( $E = 0 \text{ eV}$ ) are O 2p nonbonding orbitals. The estimated band gap is found to be around 5 eV, in good agreement with previous *ab initio* calculations [87–89]. Here, we mention that in general DFT calculations underestimate the experimental band gap of materials and our result confirms this flaw since the experimental value of the gap for silica is 9 eV [90,91].

For the interior layer of silica sandwich, one recognizes from Fig. 11(a) that its eDOS is very similar to the one of the bulk model. The main difference is that some of the peaks are less sharp and that the main bands are shifted by around 1 eV to higher energies. These results might be attributed to the protocol used to prepare the samples (sandwich geometry, quench rate). (Glass produced with a lower cooling rate is likely to be at a lower-energy state). No difference is found in the high-energy band which makes that the band gap for the sandwich geometry is reduced to 4.1 eV.

The eDOS for the interior layer of the NS5 and NS3 sandwich samples, presented in Figs. 11(b) and 11(c), are quite similar to the one for silica. Certain features do, however, depend on the composition: (1) The eDOS shifts to lower frequencies when Na is added. (2) The splitting between O  $sp$ –Si  $sp^3$  bonding and antibonding states is washed out. (3) The lowest-energy band has a new peak at around  $-17 \text{ eV}$ , and its intensity grows if the Na content increases. The

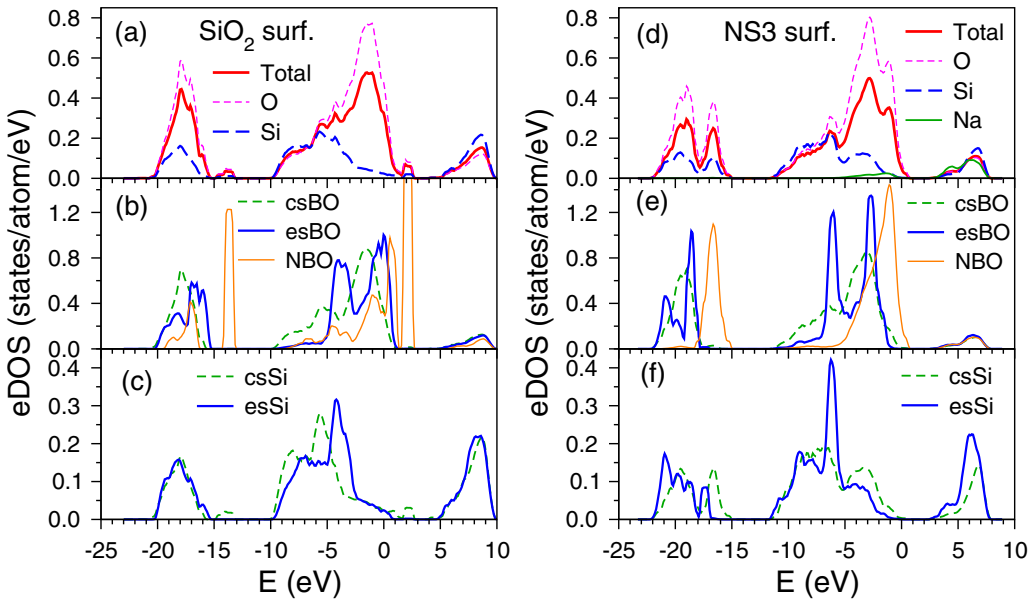


FIG. 12. Decomposition of the surface eDOS of the silica and NS3 glasses. Left panels: silica. Right panels: NS3. The Fermi level energy  $E_f$  is at 0 eV. (a), (d) Decomposition with respect to atomic species, i.e., Si, O, and Na. (b), (e) Decomposition of O into NBO, csO, and esO. (c), (f) Decomposition of Si into csSi and esSi. The eDOS are normalized with respect to the number of atoms.

observed shift of the total eDOS to lower energies for the NS5 and NS3 samples is related to the fact that the addition of Na leads to an increase of the Si-BO bond lengths (see Table II), in accordance with previous *ab initio* simulations of bulk sodium silicates [66,67,92]. This change of the Si-O bond lengths is correlated to a shift of nonbonding O $2p$  ( $-5$  to  $0$  eV) and bonding O $2s$  ( $-21$  to  $-17$  eV) orbitals to lower-energy levels, which becomes more pronounced as the Na content increases [92]. For the band below  $-15$  eV originating from O $2s$  states, we see in addition a splitting with a new peak at  $\approx -17$  eV with contributions from O $2s$  states of NBO atoms [92] (as we will also see later for our sandwich samples). We also note that the band gaps shrink with respect to the values of silica: We find  $2.9$  eV for NS5, and  $2.7$  eV for NS3. The latter two values are also compatible with the calculated band gap ( $2.8$  eV) for sodium tetrasilicate glass (i.e., 20 mol.% of Na $_2$ O) [66].

The eDOS for the surface layers do not differ strongly from their counterpart for the interior layer. The distributions at negative energies are shifted to slightly higher energies, by about 1 eV, an effect that is likely related to the presence of a larger NBO proportion (see Table III). The Si-NBO bonds being shorter than the Si-BO ones, the shift to lower energies previously mentioned will be counteracted. In addition, we find that the height of the peaks is modified, notably the ones at the lowest energies, i.e., the O $2s$  states, a result that is reasonable since in the outermost layer the structure of oxygen is quite different from the ones inside the bulk (see Fig. 2). Finally, we mention that for the case of silica the splitting between O $2p$ -Si $sp^3$  nonbonding and bonding states has vanished for the surface layer, i.e., for these energies the eDOS is now very similar to the one of the systems with sodium, an effect that is likely related to the increased structural disorder.

To get insight into the relationship between the atomic structure and the electronic properties of the glasses, we have decomposed the eDOS of the surface layers into partial contributions from the constituent atoms, i.e., Si, O, and Na [see Figs. 12(a) and 12(d)]. Subsequently, we have decomposed the eDOS of Si atoms into contributions from csSi and esSi atoms and the one of the O atoms into csBO, esBO, and NBO atoms, i.e., the species we have found to be relevant to characterize the structural properties of the samples [Figs. 12(b), 12(c), 12(e), and 12(f)]. Figures 12(a) and 12(b) show that the Si and O contribute both to the band at lowest energy, but that the distribution per atom is about three times larger for O than for Si. For the energies between  $-10$  and  $-5$  eV both species have a very similar density, as it is the case for the states with positive energy, but that the band between  $-5$  eV and the Fermi energy the signal is strongly dominated by oxygen. These results hold also for the case of NS3 [Fig. 12(d)] since we see that Na contributes basically only to the band at positive energies, i.e., the conduction band.

The further decomposition of the eDOS for the silica surface shows that the two small peaks at around  $-14$  and  $2$  eV in the total eDOS are mainly due to states of NBO atoms [see Figs. 12(b) and 12(e)], and with a weak contribution from csSi atoms [Fig. 12(c)]. Therefore, these two peaks can be assigned to Si-O dangling bonds, in agreement with the findings of previous first-principles simulations for hydrated silica [93]. These NBO give also rise to a signal at around  $-17$  eV which makes that the total eDOS for silica has a shoulder at around this energy [Fig. 12(a)], and the one for NS3 a pronounced peak [Fig. 12(d)].

For the silica surface, we note that the main valence band for the edge-sharing atoms is shifted by about 2 eV to higher energies [Fig. 12(b)]. This shift makes that the peaks and valleys in the distributions for the csBO and esBO cancel each

TABLE IV. Average Bader charge of atoms and various species found in the three glasses at 0 K. The values given in parentheses are the standard deviation of their distributions. No values in parentheses means that only one such specie has been found.

Charge ( $e$ )	Silica	NS5	NS3
Si	3.154(0.151)	3.150(0.106)	3.146(0.025)
Si <sup>3</sup>	2.458(0.469)		
Si <sup>4</sup>	3.176(0.018)	3.156(0.024)	3.146(0.025)
Si <sup>5</sup>	3.201	3.178(0.009)	3.158(0.027)
Q <sub>2</sub>	3.136	3.113(0.007)	3.105(0.017)
Q <sub>3</sub>	3.142(0.009)	3.133(0.018)	3.134(0.015)
Q <sub>4</sub>	3.177(0.018)	3.169(0.016)	3.168(0.015)
O	-1.577(0.08)	-1.586(0.055)	-1.588(0.03)
NBO	-1.106(0.243)	-1.529(0.071)	-1.543(0.01)
BO	-1.587(0.014)	-1.599(0.012)	-1.606(0.011)
esBO	-1.563(0.009)	-1.584(0.012)	-1.586(0.011)
esSi	3.144(0.013)	3.13(0.022)	3.119(0.025)
Na		0.847(0.015)	0.84(0.016)

other, resulting in a total distribution that is rather featureless, i.e., the splitting between O 2p–Si  $sp^3$  bonding and O 2p nonbonding states in the total eDOS of silica surface has disappeared [Fig. 12(a)]. The atoms of the 2M rings, i.e., esSi and esBO, give rise to peaks between -20 and -15 eV and -10 and 0 eV, features that are consistent with DFT calculation for crystalline fibrous silica containing these particular defective structures [72].

Comparing Figs. 12(b) and 12(c) for silica with the corresponding ones for NS3, Figs. 12(e) and 12(f), one sees that the various distributions are quite similar. The main difference is that the ones for NS3 are slightly shifted to lower energies. Hence, we can conclude that the corresponding shift with sodium concentration, made already in the context of Fig. 11, is due to the shift of the energies of the individual species.

### B. Bader charges

Further insight into the electronic properties of the glasses can be obtained by analyzing how the charge density can be assigned to the various type of atoms. To this aim we have employed the “atom in molecule” (AIM) approach proposed by Bader [94], which allows to partition the electron density  $\rho(\mathbf{r})$  among the constituent atoms and thus to define the atomic charges. The Bader charge is given by

$$Q_{\alpha}^{\text{Bader}} = Z_{\alpha} - \int_{V_{\text{Bader}}} \rho(\mathbf{r}) dV, \quad (3)$$

where  $Z_{\alpha}$  is the number of valence electrons of an atom  $\alpha$  and  $V_{\text{Bader}}$  is the so-called Bader volume around the atom. By definition, the Bader volume is limited by a surface  $S(\mathbf{r})$  which exhibits a zero-flux property, i.e., the inner product  $\nabla \rho(\mathbf{r}) \cdot \mathbf{n} = 0$ , where  $\mathbf{n}$  is the unit vector oriented perpendicular to  $S(\mathbf{r})$  [94].

In Table IV we list the average Bader charges of various atomic species in the three glasses. Note that, in contrast to the structural analysis, for the charge analysis we did not distinguish between the surface and interior layers since we

found no significant difference between the two. This suggests that the Bader partition scheme does not allow to establish direct relationships with the different structural and vibrational properties of the surface and interior domains (discussed in the previous sections).

For Si, the average charge of Si<sup>4</sup> (i.e., an Si bonded to four O) in the silica glass is about +3.18e, in good quantitative agreement with the result found in quartz (+3.20e) [95], in bulk amorphous silica [96], for a silver-silica interface [97], or for  $\beta$ -cristobalite surfaces [74]. In addition, we find that  $q_{\text{Si}}$  increases with increasing coordination number  $n$ , see rows Si<sup>n</sup>, in qualitative agreement with observations from a high-energy synchrotron-radiation study of stishovite (the high-pressure polymorph of silica) [98]. Furthermore, we note that  $q_{\text{Si}}$  depends also on the character of the tetrahedron  $Q_m$ , where  $m$  denotes the number of BO connected to the Si atom, in that  $q_{\text{Si}}$  increases with  $m$ . By comparing the Si charge of the three glasses, one notices that  $q_{\text{Si}}$  decreases with increasing Na concentration. An inspection of the Na dependence of the  $Q_m$  species shows that this decrease is likely due to the change in the concentration of the  $Q_n$  species and not to the Na dependence of their charge since the latter is rather weak.

For oxygen we find that the average charge of BO is close to -1.59e, a value which is in agreement with the one obtained for  $\alpha$ -quartz, -1.60e [95], and other systems containing silicon and oxygen [74,96,97]. The table also shows that  $q_{\text{BO}}$  is more negative than  $q_{\text{NBO}}$ , a deficiency of the Bader charge analysis which has already been found in previous *ab initio* simulations (see, for example, Refs. [49,89]). Despite this flaw, it is still instructive to discuss the atomic charges in different systems using the same description. Table IV shows, e.g., that the  $q_0$  becomes slightly more negative with the addition of Na. This trend is mainly due to the pronounced Na dependence of the charge of the NBO.

Regarding the 2M rings, we find that the esSi atoms are slightly less charged than the average Si atoms. This can be rationalized by the fact that in 2M rings the two oxygen atoms are quite close to each other, which makes that their electron clouds are pushed in the direction of the Si atoms, making that the charge of the latter decreases. This interpretation is coherent with the observation that the esBO have a charge that is less negative than the one of the ordinary BO.

Finally, we note that the Na charge has a value of  $\approx +0.84e$  and is basically independent of the Na concentration. This result is in good quantitative agreement with a previous *ab initio* simulation of a sodium borosilicate glass, where a Bader charge of +0.83e was found for Na ions [59].

### C. Electron localization function

In this section we discuss the nature of the chemical bonding in the glasses using the electron localization function (ELF) [100]. The ELF is related to the probability distribution  $\eta(\mathbf{r})$  of electron pairs, divided by the corresponding distribution for a uniform electron gas. By definition,  $\eta$  takes at any point of space a value that lies between 0 and 1. A value of 1 corresponds to a perfect localization of the electron pairs, while a value of 0.5 corresponds to that of a uniform electron gas. Details of the calculation can be found in Ref. [101].

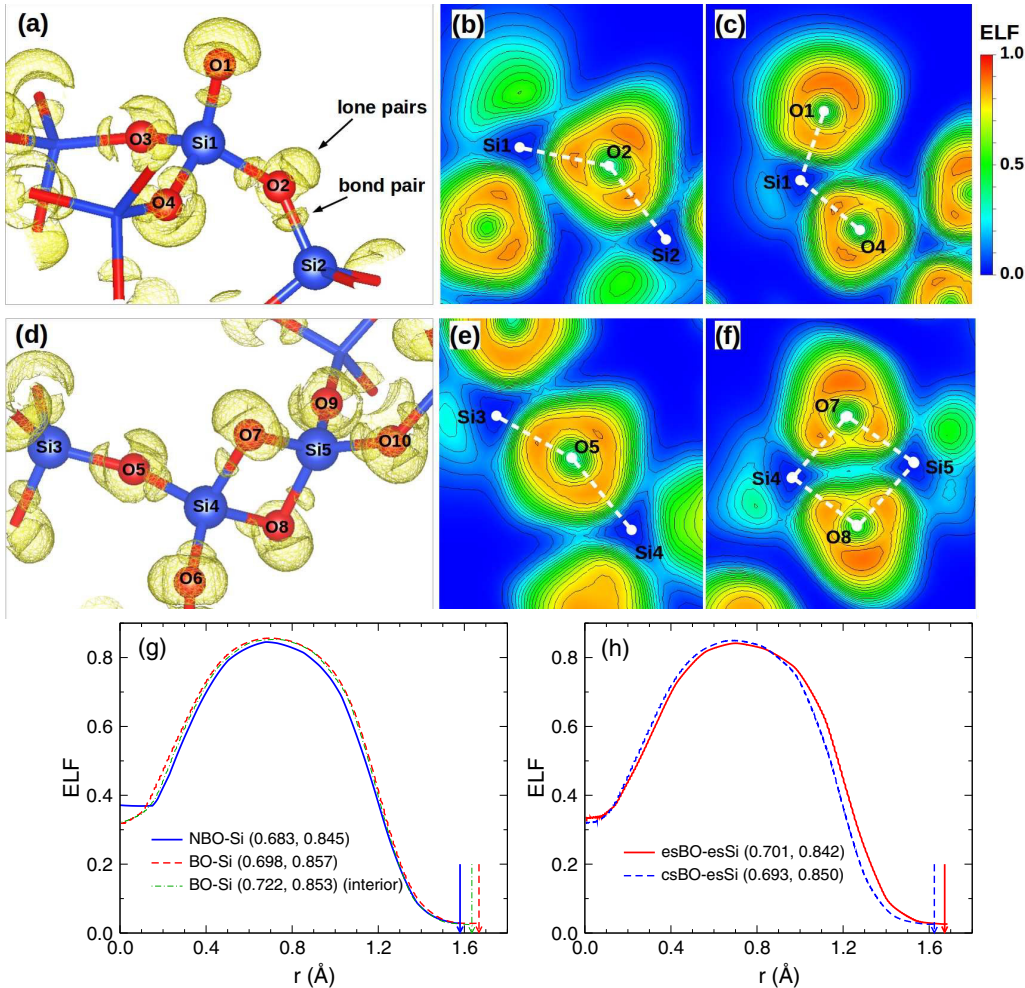


FIG. 13. Analysis of chemical bonding on a  $\text{SiO}_2$  surface by means of the electron localization function (ELF). (a) The representation of the ELF for a small region on the surface highlighting a  $\text{SiO}_4$  tetrahedron, centered on an Si atom labeled Si1, bonded to one NBO, O1, and three BO atoms (O2–O4). The isosurface (in yellow) corresponds to the ELF at a value of 0.83. (b), (c) 2D contour plots of the ELF in the planes defined by three atoms: Si1-O2-Si2 (b), and O1-Si1-O4 (c), where the atoms are identified in (a). The increment of isolines is 0.05. (d)–(f) The same representation as in (a)–(c) but for a two-membered ring structure (g), (h): line profiles of the ELF along the bond paths as shown in (a) and (d), respectively. Also included in (g) is the average ELF profile of the BO-Si bonds that belongs to a Si-BO-Si connection in the interior domain (green dashed-dotted line). The O atom is at  $r = 0$ . For each bond path the point corresponding to the maximum ELF is indicated in the parentheses [ $r$ , ELF( $r$ )]. The arrows show the location of the average Si-O bond length. The visualization of the ELF was realized by VESTA [99].

In Fig. 13 we illustrate some of the properties of the ELF for the case of the silica glass surface. Figure 13(a) shows the isosurface of the distribution evaluated at the value  $\eta = 0.83$ . The region we consider includes a  $\text{SiO}_4$  tetrahedron with one NBO (marked as O1) and three BO (O2–O4). For each BO we observe a hemispherical domain along each Si-O bond [see, for example, the bridge Si1-O2-Si2 in Fig. 13(a)], and this domain can be assigned to a pair of bonding electrons. One also finds a banana-shaped domain at the reflex side of the Si-BO-Si bridge, which is orthogonal to the Si-BO-Si plane. This domain is assigned to two lone pairs of electrons, i.e., the four valence electrons that are not involved in bonding. These nonbonding domains are substantially larger than the bonded hemispherical domains along the Si-O bonds, in agreement with the ELF mapping of the SiOSi linkage in silicate minerals [102]. For the NBO atoms, as for example the atom labeled

O1, we observe that, aside from the bond pair domain, a concave hemispherical-shaped domain can be found and it seems to have a rotational symmetry along the Si-NBO direction. This domain can be ascribed to the nonbonding electrons and it appears to have a larger volume than the nonbonding domain electron domain for BO. This observation is reasonable since presumably there are five nonbonding electrons for the NBO while only four for the BO.

Figure 13(b) shows the two-dimensional contour plot of the ELF in a plane spanned by Si1, O2, and Si2, i.e., for a BO, and, Fig. 13(c), for the plane given by O2, Si1, and O1, i.e., for a NBO. The aforementioned bonding and nonbonding domains are clearly visible from the contour plots. In addition, one recognizes from Fig. 13(c) that the probability distribution of electron pairs around the NBO is more spread out than that of the BO. This observation can be rationalized by the fact

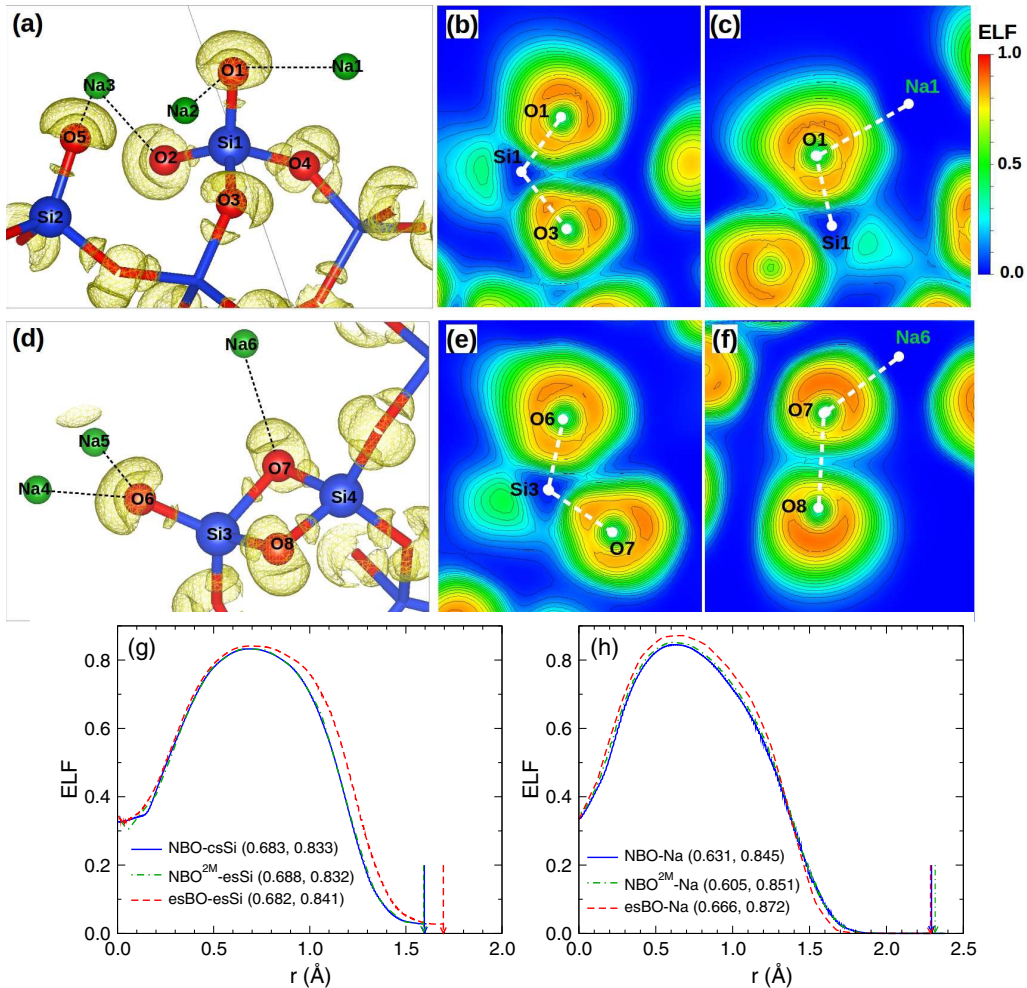


FIG. 14. Analysis of chemical bonding on the surface of NS3 by the electron localization function (ELF). (a) A map of the ELF for the structures on the surface, highlighting a  $\text{SiO}_4$  tetrahedron which has a Na in its neighborhood. The dashed lines are the O-Na bonds with  $r_{\text{O-Na}} < 2.5 \text{ \AA}$ . The isosurface represents the ELF surface at a value of 0.83 and the assignment of different domains are the same as in Fig. 13. (b), (c) 2D contour plots of the ELF in the planes defined by three atoms. The increment of isolines is 0.05. (d)–(f) The same representation as in (a)–(c) but for a two-membered ring structure. (g), (h) Line profiles of the ELF along the bond paths as shown in (a) and (d), respectively. The oxygen atom is at  $r = 0$ . For each bond path the point corresponding to the maximum ELF is indicated in the parentheses. The arrows show the location of the average Si-O or Na-O bond length. NBO<sup>2M</sup> denotes the NBO bonded to an esSi. The visualization of the ELF was realized by VESTA [99].

that the NBO has more free volume on the side opposite to the Si-O bond than the BO atoms.

A further important structural unit, namely a 2M ring, is depicted in Fig. 13(d). One notices that the O atoms in the 2M ring, O7 and O8, have electron pair domains that are similar to the ones of ordinary BO atoms, e.g., O2 in Fig. 13(a). Figures 13(e) and 13(f) show the ELF contour plots corresponding to two Si-O-Si linkages associated with the 2M ring. [Note that the Si-O-Si linkage in Fig. 13(e) involves an edge-sharing Si, Si4.] One sees that the angle Si3-O5-Si4 is much larger than the one in Fig. 13(b), demonstrating that the strong angular constraint in the 2M ring also affects the linkages of its neighbors. Consequently, the bond and lone pair domains around the BO in Fig. 13(e) are not as well structured as the ones in Fig. 13(b). Figure 13(f) shows the ELF contour plots of the 2M ring. One observes that the bond and lone pair domains are well structured and can be clearly distinguished. Another noticeable feature is that

the bond paths, i.e., the lines connecting neighboring atoms, are no longer axes of symmetry for the bond pair domains. This is likely due to the strong repulsion of the electrons from the two opposing esBO atoms.

To describe the ELF in a more quantitative manner we show in Figs. 13(g) and 13(h) the line profile of the ELF along the bond paths starting from the oxygen atom ( $r = 0$ ). Note that all BO in Figs. 13(a) and 13(g) are ordinary corner-sharing BO, i.e., csBO. Figure 13(g) shows that the ELF of the NBO-Si bond is smaller than the one of the BO-Si bond, implying that the ELF around the NBO is more spread out, in agreement with the contour plot in Fig. 13(c). In addition, we note that the BO-Si bond peaks at a larger  $r$  than the Si-NBO bond (see the values in the parentheses of the legend), in agreement with the observation that for the NBO the ELF is extended in the direction opposite to the Si-O bond. Also included in Fig. 13(g) is the ELF profile corresponding to a Si-BO-Si linkage in the interior of the sample and which has

an angle close to the Si1-O2-Si2 linkage shown in Fig. 13(a). The presence of the surface does not seem to affect in a significant manner the ELF profile of the Si-BO bonds, although the BO-Si bond length (indicated by the vertical arrows) in the interior is slightly smaller than the surface BO-Si (see also Table II). Figure 13(h) compares the ELF line profiles of the esBO-esSi and csBO-esSi bonds and one notices that the ELF of the esBO-esSi bonds shifts to a larger  $r$  relative to the csBO-esSi bonds but seems to have the same maximum height. However, since for the esBO-esSi bond the bond path does not pass through the maximum of the ELF [see Fig. 13(f)], the real maximum value of the ELF for this bond is in fact higher than the one for the csBO-esSi bond, i.e., the electrons are more localized.

Figure 14 shows the ELF results for the NS3 glass surface. We note that, in addition to the structural modification discussed in the previous sections, the presence of Na induces also changes in the bonding. For example, Fig. 14(a), the bond pair domain for the NBO-Si bond O1-Si1 is much smaller than the corresponding domain in silica [Fig. 13(a)]. Figure 14(b) shows that the presence of Na also leads to an asymmetry of the lone pair domain of the NBO (i.e., O1). This effect is also seen from the two-dimensional (2D) contour plot in the plane defined by Na1-O1-Si1 [Fig. 14(c)]. For the NBO, O1, we note that the domains in the directions of the Na atoms can be ascribed to the Na-O bond pair interaction superimposed on the lone pair domains [Fig. 14(c)]. Similar results were found for earth materials containing alkali metals [102].

Figure 14(d) shows a 2M ring with one of the Si atoms connected to a NBO and its nearby Na atoms. Figure 14(e) shows that, for the 2M rings, the distribution is no longer symmetric around the O7(esBO)-Si3 connection, an observation that is coherent with the finding for the 2M rings in silica (see Fig. 13). For the NBO, O6, we find that the ELF contour plot is quite similar to the one for O1 shown in Fig. 14(b), in spite of the presence of the neighboring 2M ring. Figure 14(f) clearly shows that the ELF for the esBO (O7) bonded to the Na is less spread out than the distribution for the other esBO (O8) in the 2M ring, demonstrating that O7 is indeed bonded to the Na atom.

Figure 14(g) shows the average ELF line profiles of various types of O-Si bonds. (Note that the NBO atom connected to an esSi atom is denoted as NBO<sup>2M</sup>.) One observes that the ELF profile of the NBO-csSi bond is very similar to the one of the NBO<sup>2M</sup>-esSi bond, indicating that the NBO-Si bond character is basically independent of the Si type. Furthermore, we find that the ELF values of the NBO-Si bonds are smaller than that of the esBO-esSi bond, in accordance with the fact that the distribution of the electron pairs around the NBO is more spread out than the one for the esBO-esSi bond. (Also here we recall that the ELF for the esBO-esSi is not symmetric with respect to the connecting axis [see Fig. 14(c)], and hence the maximum value is even higher). For all the three NBO-Si bonds, the maximum of the ELF is located at  $r \approx 0.68$  Å, independent of the bond type. Figure 14(h) shows the profiles for the O-Na pairs and one sees that the maxima of the curves are located at  $r \approx 0.61$ , 0.63, and 0.67 Å for the NBO<sup>2M</sup>-Na, NBO-Na, and esBO-Na bonds, respectively. These results indicate that the character of the O-Na bond is more sensitive to the changes in local environment than the NBO-Si bond. We

also note that the maxima of the ELF for the O-Na bonds are closer to the oxygen atoms (at  $r = 0$ ) than the ones of the O-Si bonds. This result demonstrates that the O-Na is less covalent (i.e., more ionic) than the O-Si bonds. In addition, based on the locations of the ELF maxima, it can be deduced that the esBO-Na bond is more covalent than the NBO-Na bonds.

Finally, we note that the locations of the maxima of the ELF profiles for the NBO-Si and esBO-esSi bonds are very close to the corresponding values found for the silica glass. This similarity indicates that the presence of Na affects the position of the bond pair domains of the O-Si bonds only weakly.

## VI. SUMMARY AND CONCLUSIONS

Using *ab initio* calculations, we have studied the structural, vibrational, and electronic properties of the surface of amorphous silica and two binary sodasilicate glasses. Previous studies have shown that, for the case of silica, two-membered rings are an important structural motif at the surface [22,23]. The present analysis of the compositional dependence of the surface and interior domains of our sandwich samples shows that the concentration of defect sites is considerably reduced with increasing Na content since sodium migrates from the interior to the surface and transforms energetically unfavorable local structures, such as 2M rings, into more relaxed ones. As a consequence, the concentration of two-membered rings decreases rapidly with the addition of sodium.

From the dynamical matrix of the samples we have calculated the total vibrational density of states as well as the contributions of the various atomic species and structural elements to this distribution. This has allowed us to identify the spectroscopic signatures of the 2M rings and see how these change as a function of the sodium content. In addition, we have computed the IR spectra and have also determined for this observable the signature of the 2M rings. These calculations show that not all vibrational modes of the 2M rings are IR active, thus pointing out the need to use additional experimental techniques to study these rings. In addition, this study can serve as a benchmark for simulations of glass surfaces using effective potentials since our results will allow to compare the results of the classical MD simulations with highly accurate microscopic structural and vibrational data.

Taking advantage of the *ab initio* approach, we have probed the electronic properties of the glass samples with a particular focus on the surfaces. The analysis of the electron localization function shows that 2M rings and NBO do have a distinct electronic distribution and we have investigated how it is affected by the presence of sodium. The current simulations and analysis represent a study that investigates simultaneously the structural, spectroscopic, and electronic properties of silica glass surface and how they evolve with Na addition. Hence, this approach allows to circumvent the frequently encountered problem that the samples probed with different techniques usually have different production histories (cooling rates, composition, atmospheres, etc.) which makes the unambiguous identification of the various structural features difficult. As a consequence, this work should be a relevant step forward in our understanding of the properties of oxide glasses on a quantitative level.

## ACKNOWLEDGMENTS

Z.Z. acknowledges financial support by China Scholarship Council (Grant No. 201606050112). W.K. is member of the Institut Universitaire de France. This work was granted ac-

- cess to the HPC resources of CINES attributed by GENCI (Grand Equipement National de Calcul Intensif) under the allocation Grants No. A0030907572, No. A0050907572, and No. A0070907572.
- 
- [1] C. G. Pantano, Glass surfaces, in *Current Trends in the Science and Technology of Glass*, edited by H. Jain, A. R. Cooper, K. J. Rao, and D. Chakravorty (World Scientific, 1989), pp. 159–180.
- [2] P. Bocko, P. Fenn, L. Morse, and F. Okamoto, Surface chemistry and microstructure of flat panel display substrates, *SID 91 Digest* (Society for Information Display, 1991), Vol. 675.
- [3] H. Bach, Advanced surface analysis of silicate glasses, oxides and other insulating materials: A review, *J. Non-Cryst. Solids* **209**, 1 (1997).
- [4] L. T. Zhuravlev, The surface chemistry of amorphous silica. Zhuravlev model, *Colloids Surf., A* **173**, 1 (2000).
- [5] A. Pugliara, K. Makasheva, B. Despax, M. Bayle, R. Carles, P. Benzo, G. BenAssayag, B. Pécassou, M. C. Sancho, E. Navarro *et al.*, Assessing bio-available silver released from silver nanoparticles embedded in silica layers using the green algae chlamydomonas reinhardtii as bio-sensors, *Sci. Total Environ.* **565**, 863 (2016).
- [6] T. Dey and D. Naughton, Cleaning and anti-reflective (AR) hydrophobic coating of glass surface: A review from materials science perspective, *J. Sol-Gel Sci. Technol.* **77**, 1 (2016).
- [7] K. Zheng, M. Kapp, and A. R. Boccaccini, Protein interactions with bioactive glass surfaces: A review, *Appl. Mater. Today* **15**, 350 (2019).
- [8] T. L. Anderson, *Fracture Mechanics: Fundamentals and Applications, Fourth Edition* (CRC Press, Boca Raton, FL, 2017).
- [9] Z. Zhang, S. Ispas, and W. Kob, Structure and vibrational properties of sodium silicate glass surfaces, *J. Chem. Phys.* **153**, 124503 (2020).
- [10] J. F. Kelso, C. G. Pantano, and S. H. Garofalini, A comparison of ion scattering spectra and molecular dynamics simulations at the surface of silicate glasses, *Surf. Sci. Lett.* **134**, L543 (1983).
- [11] R. M. Almeida, R. Hickey, H. Jain, and C. G. Pantano, Low-Energy Ion Scattering spectroscopy of silicate glass surfaces, *J. Non-Cryst. Solids* **385**, 124 (2014).
- [12] R. M. Almeida, H. Jain, and C. G. Pantano, Low-Energy Ion-Scattering Spectroscopy of Modified Silicate Glasses, *J. Am. Ceram. Soc.* **99**, 1259 (2016).
- [13] C. V. Cushman, P. Brüner, J. Zakel, C. Dahlquist, B. Sturgell, T. Grehl, B. M. Lunt, J. Banerjee, N. J. Smith, and M. R. Linford, Low energy ion scattering (LEIS) of as-formed and chemically modified display glass and peak-fitting of the Al/Si LEIS peak envelope, *Appl. Surf. Sci.* **455**, 18 (2018).
- [14] E. Rädlein and G. H. Frischat, Atomic force microscopy as a tool to correlate nanostructure to properties of glasses, *J. Non-Cryst. Solids* **222**, 69 (1997).
- [15] J.-F. Poggemann, A. Goss, G. Heide, E. Rädlein, and G. Frischat, Direct view of the structure of a silica glass fracture surface, *J. Non-Cryst. Solids* **281**, 221 (2001).
- [16] J.-F. Poggemann, G. Heide, and G. Frischat, Direct view of the structure of different glass fracture surfaces by atomic force microscopy, *J. Non-Cryst. Solids* **326**, 15 (2003).
- [17] G. Frischat, J.-F. Poggemann, and G. Heide, Nanostructure and atomic structure of glass seen by atomic force microscopy, *J. Non-Cryst. Solids* **345**, 197 (2004).
- [18] V. Radzig, Point defects on the silica surface: Structure and reactivity, *Thin Films Nanostruct.* **34**, 231 (2007).
- [19] P. Berruyer, M. Lelli, M. P. Conley, D. L. Silverio, C. M. Widdifield, G. Siddiqi, D. Gajan, A. Lesage, C. Copéret, and L. Emsley, Three-dimensional structure determination of surface sites, *J. Am. Chem. Soc.* **139**, 849 (2017).
- [20] A. Comas-Vives, K. Larmier, and C. Copéret, Understanding surface site structures and properties by first principles calculations: An experimental point of view! *Chem. Commun.* **53**, 4296 (2017).
- [21] A. K. Varshneya, *Fundamentals of Inorganic Glasses* (Elsevier, Amsterdam, 2013).
- [22] A. Rimola, D. Costa, M. Sodupe, J.-F. Lambert, and P. Ugliengo, Silica Surface Features and Their Role in the Adsorption of Biomolecules: Computational Modeling and Experiments, *Chem. Rev.* **113**, 4216 (2013).
- [23] F. Tielens, M. Gierada, J. Handzlik, and M. Calatayud, Characterization of amorphous silica based catalysts using dft computational methods, *Catal. Today* **354**, 3 (2019).
- [24] B. Morrow and I. Cody, Infrared studies of reactions on oxide surfaces. 5. Lewis acid sites on dehydroxylated silica, *J. Phys. Chem.* **80**, 1995 (1976).
- [25] B. Bunker, D. Haaland, K. Ward, T. Michalske, W. Smith, J. S. Binkley, C. Melius, and C. Balfe, Infrared spectra of edge-shared silicate tetrahedra, *Surf. Sci.* **210**, 406 (1989).
- [26] A. Grabbe, T. Michalske, and W. Smith, Strained siloxane rings on the surface on silica: Their reaction with organosiloxanes, organosilanes, and water, *J. Phys. Chem.* **99**, 4648 (1995).
- [27] C. Copéret, M. Chabanas, R. Petroff Saint-Arroman, and J.-M. Basset, Homogeneous and heterogeneous catalysis: Bridging the gap through surface organometallic chemistry, *Angew. Chem. Inter. Ed.* **42**, 156 (2003).
- [28] P. Šot, C. Copéret, and J. A. Van Bokhoven, Fully dehydroxylated silica generated from hydrosilane: Surface defects and reactivity, *J. Phys. Chem. C* **123**, 23480 (2019).
- [29] A. M. Ferrari, E. Garrone, G. Spoto, P. Ugliengo, and A. Zecchina, Reactions of silica strained rings: An experimental and ab-initio study, *Surf. Sci.* **323**, 151 (1995).
- [30] L. Vaccaro, M. Cannas, V. Radzig, and R. Boscaino, Luminescence of the surface nonbridging oxygen hole center in silica: Spectral and decay properties, *Phys. Rev. B* **78**, 075421 (2008).
- [31] S. H. Garofalini, A molecular dynamics simulation of the vitreous silica surface, *J. Chem. Phys.* **78**, 2069 (1983).
- [32] B. P. Feuston and S. H. Garofalini, Topological and bonding defects in vitreous silica surfaces, *J. Chem. Phys.* **91**, 564 (1989).

- [33] S. H. Garofalini, Molecular dynamics computer simulations of silica surface structure and adsorption of water molecules, *J. Non-Cryst. Solids* **120**, 1 (1990).
- [34] M. Wilson and T. R. Walsh, Hydrolysis of the amorphous silica surface. I. structure and dynamics of the dry surface, *J. Chem. Phys.* **113**, 9180 (2000).
- [35] A. Roder, W. Kob, and K. Binder, Structure and dynamics of amorphous silica surfaces, *J. Chem. Phys.* **114**, 7602 (2001).
- [36] M. Ravivomanantsoa, P. Jund, and R. Jullien, Classical molecular dynamics simulations of amorphous silica surfaces, *J. Phys.: Condens. Matter* **13**, 6707 (2001).
- [37] C. Wang, N. Kuzu, and Y. Tamai, Molecular dynamics study on surface structure of a-SiO<sub>2</sub> by charge equilibration method, *J. Non-Cryst. Solids* **318**, 131 (2003).
- [38] J. Du and A. N. Cormack, Molecular dynamics simulation of the structure and hydroxylation of silica glass surfaces, *J. Am. Ceram. Soc.* **88**, 2532 (2005).
- [39] W. Gonçalves, J. Morthomas, P. Chantrenne, M. Perez, G. Foray, and C. L. Martin, Molecular dynamics simulations of amorphous silica surface properties with truncated coulomb interactions, *J. Non-Cryst. Solids* **447**, 1 (2016).
- [40] J. M. Rimsza, R. E. Jones, and L. J. Criscenti, Surface structure and stability of partially hydroxylated silica surfaces, *Langmuir* **33**, 3882 (2017).
- [41] S. Halbert, S. Ispas, C. Raynaud, and O. Eisenstein, Modelling the surface of amorphous dehydroxylated silica: The influence of the potential on the nature and density of defects, *New J. Chem.* **42**, 1356 (2018).
- [42] S. H. Garofalini and S. Levine, Differences in surface behavior of alkali ions in Li<sub>2</sub>O · 3SiO<sub>2</sub> and Na<sub>2</sub>O · 3SiO<sub>2</sub> glasses, *J. Am. Ceram. Soc.* **68**, 376 (1985).
- [43] M. Ren, L. Deng, and J. Du, Surface structures of sodium borosilicate glasses from molecular dynamics simulations, *J. Am. Ceram. Soc.* **100**, 2516 (2017).
- [44] S. H. Garofalini, M. T. Ha, and J. Urraca, Simulations of the surfaces of soda lime aluminoborosilicate glasses exposed to water, *J. Am. Ceram. Soc.* **101**, 1135 (2018).
- [45] G. Agnello, L. Wang, N. Smith, R. Manley, and A. Cormack, Structure of cas glass surfaces and electrostatic contact charging behavior: A joint simulation and experimental investigation, *Int. J. Appl. Glass Sci.* **12**, 111 (2021).
- [46] W. Kob and S. Ispas, First-principles simulations of glass-formers, in *Encyclopedia of Glass Science, Technology, History, and Culture*, edited by P. Richet (Wiley, Hoboken, NJ, 2020), pp. 201–213.
- [47] N. P. Bansal and R. H. Doremus, *Handbook of Glass Properties* (Academic, Orlando, 1986).
- [48] Z. Zhang, Fracture, surface, and structure of silicate glasses: Insights from atomistic computer simulations, Ph.D. thesis, University of Montpellier, 2020.
- [49] L. Pedesseau, S. Ispas, and W. Kob, First-principles study of a sodium borosilicate glass-former. II. The glass state, *Phys. Rev. B* **91**, 134202 (2015).
- [50] G. Kresse and J. Furthmüller, Efficiency of *ab-initio* total energy calculations for metals and semiconductors using a plane-wave basis set, *Comput. Mater. Sci.* **6**, 15 (1996).
- [51] G. Kresse and J. Furthmüller, Efficient iterative schemes for *ab initio* total-energy calculations using a plane-wave basis set, *Phys. Rev. B* **54**, 11169 (1996).
- [52] W. Kohn and L. J. Sham, Self-consistent equations including exchange and correlation effects, *Phys. Rev.* **140**, A1133 (1965).
- [53] R. M. Martin, *Electronic Structure: Basic Theory and Practical Methods* (Cambridge University Press, Cambridge, 2004).
- [54] J. P. Perdew, K. Burke, and M. Ernzerhof, Generalized Gradient Approximation Made Simple, *Phys. Rev. Lett.* **77**, 3865 (1996).
- [55] J. P. Perdew, A. Ruzsinszky, G. I. Csonka, O. A. Vydrov, G. E. Scuseria, L. A. Constantin, X. Zhou, and K. Burke, Restoring the Density-Gradient Expansion for Exchange in Solids and Surfaces, *Phys. Rev. Lett.* **100**, 136406 (2008).
- [56] P. E. Blöchl, Projector augmented-wave method, *Phys. Rev. B* **50**, 17953 (1994).
- [57] G. Kresse and D. Joubert, From ultrasoft pseudopotentials to the projector augmented-wave method, *Phys. Rev. B* **59**, 1758 (1999).
- [58] S. Nosé, A molecular dynamics method for simulations in the canonical ensemble, *Mol. Phys.* **52**, 255 (1984).
- [59] L. Pedesseau, S. Ispas, and W. Kob, First-principles study of a sodium borosilicate glass-former. I. The liquid state, *Phys. Rev. B* **91**, 134201 (2015).
- [60] S. Sundararaman, L. Huang, S. Ispas, and W. Kob, New optimization scheme to obtain interaction potentials for oxide glasses, *J. Chem. Phys.* **148**, 194504 (2018).
- [61] S. Sundararaman, L. Huang, S. Ispas, and W. Kob, New interaction potentials for alkali and alkaline-earth aluminosilicate glasses, *J. Chem. Phys.* **150**, 154505 (2019).
- [62] T. Mahadevan and J. Du, Hydration and reaction mechanisms on sodium silicate glass surfaces from molecular dynamics simulations with reactive force fields, *J. Am. Ceram. Soc.* **103**, 3676 (2020).
- [63] T. A. Michalske and B. Bunker, Slow fracture model based on strained silicate structures, *J. Appl. Phys.* **56**, 2686 (1984).
- [64] L. H. Dubois and B. R. Zegarski, Bonding of alkoxy silanes to dehydroxylated silica surfaces: A new adhesion mechanism, *J. Phys. Chem.* **97**, 1665 (1993).
- [65] L. H. Dubois and B. R. Zegarski, Reaction of alkoxy silane coupling agents with dehydroxylated silica surfaces, *J. Am. Chem. Soc.* **115**, 1190 (1993).
- [66] S. Ispas, M. Benoit, P. Jund, and R. Jullien, Structural and electronic properties of the sodium tetrasilicate glass Na<sub>2</sub>Si<sub>4</sub>O<sub>9</sub> from classical and *ab initio* molecular dynamics simulations, *Phys. Rev. B* **64**, 214206 (2001).
- [67] A. Tilcock and N. H. de Leeuw, Structural and electronic properties of modified sodium and soda-lime silicate glasses by car-parrinello molecular dynamics, *J. Mater. Chem.* **16**, 1950 (2006).
- [68] F. Angeli, O. Villain, S. Schuller, S. Ispas, and T. Charpentier, Insight into sodium silicate glass structural organization by multinuclear NMR combined with first-principles calculations, *Geochim. Cosmochim. Acta* **75**, 2453 (2011).
- [69] D. Kiliyimis, S. Ispas, B. Hehlen, S. Peuget, and J.-M. Delaye, Vibrational properties of sodosilicate glasses from first-principles calculations, *Phys. Rev. B* **99**, 054209 (2019).
- [70] A. C. Wright, Neutron scattering from vitreous silica. V. the structure of vitreous silica: What have we learned from 60 years of diffraction studies? *J. Non-Cryst. Solids* **179**, 84 (1994).

- [71] A. Comas-Vives, Amorphous SiO<sub>2</sub> surface models: Energetics of the dehydroxylation process, strain, ab initio atomistic thermodynamics and ir spectroscopic signatures, *Phys. Chem. Chem. Phys.* **18**, 7475 (2016).
- [72] D. R. Hamann, Energies of strained silica rings, *Phys. Rev. B* **55**, 14784 (1997).
- [73] M. O'Keeffe and G. Gibbs, Defects in amorphous silica: *Ab initio* MO calculations, *J. Chem. Phys.* **81**, 876 (1984).
- [74] H.-L. T. Le, J. Goniakowski, C. Noguera, A. Koltsos, and J.-M. Mataigne, Structural, electronic and adhesion characteristics of zinc/silica interfaces: *Ab initio* study on zinc/β-cristobalite, *Phys. Chem. Chem. Phys.* **20**, 6254 (2018).
- [75] C. M. Chiang, B. R. Zegarski, and L. H. Dubois, First observation of strained siloxane bonds on silicon oxide thin films, *J. Phys. Chem.* **97**, 6948 (1993).
- [76] H. Edelsbrunner and E. P. Mücke, Three-dimensional alpha shapes, *ACM Trans. Graphics* **13**, 43 (1994).
- [77] A. Stukowski, Visualization and analysis of atomistic simulation data with OVITO - the Open Visualization Tool, *Model. Simul. Mater. Sci. Eng.* **18**, 015012 (2010).
- [78] N. Zotov, I. Ebbsjö, D. Timpel, and H. Keppler, Calculation of Raman spectra and vibrational properties of silicate glasses: Comparison between Na<sub>2</sub>Si<sub>4</sub>O<sub>9</sub> and SiO<sub>2</sub> glasses, *Phys. Rev. B* **60**, 6383 (1999).
- [79] S. Bromley, M. Zwijnenburg, and T. Maschmeyer, Two-ring vibrational modes on silica surfaces investigated via fully coordinated nanoclusters, *Surf. Sci.* **539**, L554 (2003).
- [80] D. Ceresoli, M. Bernasconi, S. Iarlari, M. Parrinello, and E. Tosatti, Two-Membered Silicon Rings on the Dehydroxylated Surface of Silica, *Phys. Rev. Lett.* **84**, 3887 (2000).
- [81] H. Philipp, Silicon dioxide (SiO<sub>2</sub>) (glass), in *Handbook of Optical Constants of Solids*, edited by D. Palik (Academic, San Diego, 1998), pp. 749–763.
- [82] M. De La Pierre, R. Demichelis, and R. Dovesi, Vibrational spectroscopy of minerals through ab initio methods, in *Molecular Modeling of Geochemical Reactions: An Introduction*, edited by J. D. Kubicki (Wiley, Chichester, 2016), p. 341.
- [83] C. I. Merzbacher and W. B. White, Structure of Na in aluminosilicate glasses: A far-infrared reflectance spectroscopic study, *Am. Mineral.* **73**, 1089 (1988).
- [84] J. A. Kapoutsis, E. I. Kamitsos, G. D. Chryssikos, Y. D. Yiannopoulos, A. P. Patsis, and M. Prassas, Alkali sites in silicate glasses, *Chim. Chronica New Series* **23**, 341 (1994).
- [85] M. D. Ingram, J. E. Davidson, A. M. Coats, E. I. Kamitsos, and J. A. Kapoutsis, Origins of anomalous mixed-alkali effects in ion-exchanged glasses, *Glass Sci. Technol. Glastech. Ber.* **73**, 89 (2000).
- [86] S. Ispas (private communication).
- [87] J. Sarnthein, A. Pasquarello, and R. Car, Model of vitreous SiO<sub>2</sub> generated by an *ab initio* molecular-dynamics quench from the melt, *Phys. Rev. B* **52**, 12690 (1995).
- [88] M. Benoit, S. Ispas, P. Jund, and R. Jullien, Model of silica glass from combined classical and ab initio molecular-dynamics simulations, *Eur. Phys. J. B* **13**, 631 (2000).
- [89] J. Du and L. R. Corrales, Structure, dynamics, and electronic properties of lithium disilicate melt and glass, *J. Chem. Phys.* **125**, 114702 (2006).
- [90] F. J. Himpsel and D. Straub, Inverse photoemission as a probe for unoccupied electronic states, *Surf. Sci.* **168**, 764 (1986).
- [91] F. J. Grunthaner and P. J. Grunthaner, Chemical and electronic structure of the SiO<sub>2</sub>/Si interface, *Mater. Sci. Rep.* **1**, 65 (1986).
- [92] R. Murray and W. Ching, Electronic structure of sodium silicate glasses, *J. Non-Cryst. Solids* **94**, 144 (1987).
- [93] M. Benoit, M. Pöhlmann, and W. Kob, On the nature of native defects in high OH-content silica glasses: A first-principles study, *Europhys. Lett.* **82**, 57004 (2008).
- [94] R. F. Bader, *Atoms in Molecule: A Quantum Theory* (Oxford University Press, Oxford, 1985).
- [95] G. V. Gibbs, K. M. Rosso, D. M. Teter, M. B. Boisen Jr, and M. S. T. Bukowinski, Model structures and properties of the electron density distribution for low quartz at pressure: A study of the SiO bond, *J. Mol. Struct.* **485**, 13 (1999).
- [96] A. Pasquarello and R. Car, Dynamical Charge Tensors and Infrared Spectrum of Amorphous SiO<sub>2</sub>, *Phys. Rev. Lett.* **79**, 1766 (1997).
- [97] H. Balout, N. Tarrat, J. Puibasset, S. Ispas, C. Bonafos, and M. Benoit, Density functional theory study of the spontaneous formation of covalent bonds at the silver/silica interface in silver nanoparticles embedded in SiO<sub>2</sub>: Implications for Ag<sup>+</sup> release, *ACS Appl. Nano Mater.* **2**, 5179 (2019).
- [98] A. Kirfel, H.-G. Krane, P. Blaha, K. Schwarz, and T. Lippmann, Electron-density distribution in stishovite, SiO<sub>2</sub>: A new high-energy synchrotron-radiation study, *Acta Crystallogr., Sect. A: Found. Crystallogr.* **57**, 663 (2001).
- [99] K. Momma and F. Izumi, VESTA 3 for three-dimensional visualization of crystal, volumetric and morphology data, *J. Appl. Crystallogr.* **44**, 1272 (2011).
- [100] A. D. Becke and K. E. Edgecombe, A simple measure of electron localization in atomic and molecular systems, *J. Chem. Phys.* **92**, 5397 (1990).
- [101] A. Savin, R. Nesper, S. Wengert, and T. F. Fässler, ELF: The Electron Localization Function, *Angew. Chem. Inter. Ed.* **36**, 1808 (1997).
- [102] G. V. Gibbs, D. F. Cox, N. L. Ross, T. D. Crawford, J. B. Burt, and K. M. Rosso, A mapping of the electron localization function for earth materials, *Phys. Chem. Miner.* **32**, 208 (2005).